Orbital characterization of iron-pnictide high-temperature superconductors by angle resolved photoemission spectroscopy

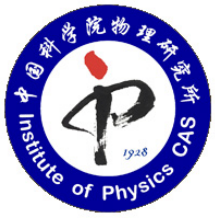

Laurent Cevey
Photoelectron Spectroscopy Research Group EX7
Beijing Institute of Physics, Chinese Academy of Science

Master Thesis
Supervisor: Pr. Hong Ding
EPFL Supervisor: Pr. Henrik M. Rønnow

August 20, 2010

Abstract

The electronic structure of the optimally hole-doped pnictide compound $Ba_{0.6}K_{0.4}Fe_2As_2$ was obtained and studied by angle resolved photoemission spectroscopy (ARPES). The light polarization dependence of the bands is explained by the selection rules contained in the photoemission transition matrix elements, and gives novel information on the possible orbital character of the bands. The Fermi surface geometry also shows important variations with light polarization. An attempt is made to analyze its more complex link with the selection rules by making a comparison with Fermi surface orbital character simulations. While some good correspondence can be observed, a number of inconstistancies and a large photon energy dependence seems to underline the importance of the more global matrix elements.

Acknowledgments

I would like to express my utmost gratitude to Professor Hong Ding for accepting me to write my Master thesis at EX7, Beijing Institute of Physics, for offering me the opportunity to learn ARPES and actively take part in exciting state-of-the-art research on iron pnictides, and for his guidance all along my project.

I also wish to thank my fellow students and professors from the group, especially Xiaoping Wang, Yaobo Huang, Nan Xu, professor Tian Qian and professor Jing Dong for all the enlightening discussions and enjoyable times spent working together in the laboratory. I am also grateful to Ms. Mu Li for her help with daily administrative issues, and to Pierre Richard who reviewed and corrected my thesis.

Last but not least, I would like to greatly thank Henrik Ronnow for being my EPFL supervisor and for putting me through Professor Ding. Without his original support and enthusiasm in finding a suitable research group in China, this work would not have existed.

Contents

Introduction

The project

This thesis presents an overview of a project conducted at the Institute of Physics (IOP), Chinese Academy of Science (CAS) in Beijing for the obtention of the Ecole Polytechnique Federale de Lausanne (EPFL) Master degree in physics. This project is the result of an exchange program between the Laboratory of Quantum Magnetism (LQM) at EPFL and the EX7 Photoelectron Spectroscopy Research Group at IOP, and was conducted in the latter.

The objectives of this work were multiple. This project represented a unique exchange opportunity in a young promissing laboratory, not only leader of ARPES in China, but also with good international imprint. The original goal was to take part in experiments on novel iron pnictides samples from the high temperature superconductors family, thereby understanding the stakes of such a striving research field. Moreover, a solid formation in the powerful angle resolved photoemission spectroscopy (ARPES) technique was also acquired while working on a state-of-the-art ARPES equipment. Experience was gained from assisting different projects within the group and by solving the numerous technical issues met all along the project. Extensive reference exploration of the iron pnictides current state of research and present issues was also carried out, thereby completing and comparing the views and scenarios supported by our laboratory with those of other groups.

As a concretisation of the preceding formation and studies, an example study of the respectively electron and hole doped novel compounds $BaFe_{1.9}Pt_{0.1}As_2$ and $NaFeAs_{0.8}P_{0.2}$ is presented, followed by a detailed study of the orbital character of the optimally doped $Ba_{0.6}K_{0.4}Fe_2As_2$ compound. This research is based on data gathered during experiments conducted in several facilities: our EX7 laboratory, Professor Takahashi's ARPES laboratory at Tohoku University, and the ARPES system of the Surface and Interface Spectroscopy (SIS) X09LA beamline at the Swiss Light Source (SLS) synchrotron. The main experiment on $Ba_{0.6}K_{0.4}Fe_2As_2$ was conducted in the latter with my personal implication.

The structure of the thesis follows the objectives presented above: a first part will give a "digest" of the current state of research on iron pnictides. In particular, the controversial topics of superconducting gap symmetry, Fermi surface orbital character, nature of magnetism and spin resonance will be discussed in conceptual terms, while a subsequent part will present

specific theoretical models. The second part will present the ARPES technique, from the basic theoretical considerations to the details of the experimental setup. In the last part the results obtained will be presented and discussed.

High temperature superconductivity

Before entering the details of the ARPES application to pnictides, it is good to review some principles of superconductivity and of the later discovered family of high temperature superconductors.

The long known phenomenon of superconductivity — the sudden disappearance of electrical resistivity below a critical temperature T_c — was successfully explained by the *Bardeen-Cooper-Schrieffer* (BCS) theory in 1957. At least it was believed by all until very recently[1]. Under a certain temperature in the superconducting materials, a favourable energy configuration due to interaction with phonons lets electrons of energy close to the Fermi energy and of opposite momentum pair up and collapse into a bose condensate. However, this scheme with phonons as the main actors of the superconducting phenomenon presented a limit with the prediction of a highest possible transition temperature $T_c^{max} \approx 30\,\mathrm{K}$[2].

The discovery in 1986 of so-called *high-temperature superconductivity* (HTS) by Bednorz and Müller [1] in a material superconducting at $T_c \approx 35\,\mathrm{K}$ thus challenged the established knowledge of the BCS theory. The enthusiastic wave of research that followed that discovery quickly pointed out several exotic properties of these materials. First, while they conduct electrons without resistance below their critical temperature, the ground state of their parent compound is a Mott insulator, with strong interactions between the localized electron and displaying antiferromagnetism. Second, the superconducting gap is anisotropic with a d-wave symmetry, in contrast with the isotropic s-wave gap of conventional superconductors. Last, the complex phenomena in the cuprates — mainly due to strong electron-electron interactions — is combined with a layered crystal structure which has two advantages. Indeed, it leads to a quasi two-dimensional electronic structure and a natural cleavage plane, which simplifies the treatment of experimental results that can be conveniently obtained from surface-sensitive probes like ARPES and tunneling electron microscopy.

Apart from the cuprates, other unconventional superconductor families include heavy-fermion superconductors, ruthenates and organic superconductors. The label *unconventional* is often related to the symmetry of the superconducting order parameter, namely it denotes supercon-

[1] In 2009, some opinions [2] came up arguing the possible invalidity of the BCS theory in describing even conventional superconductivity. The paper argues that most of the unconventional superconductors, as well as several superconducting properties — surprisingly, according to the author, these include the *Meissner effect* — are not well explained by the BCS theory. The whole theory might thereby need to be revised. These arguments seem however quite unreliable.

[2] later lifted up to $T_c^{max'} \approx 55\,\mathrm{K}$, after for instance the discovery of conventional superconductors like MgB_2 superconducting at 39 K, due to a particular phonon mode.

ductors in which this symmetry is lower than that of the lattice [3]. While the research on cuprates has recently celebrated its 20th birthday, the HTS research was revitalized with the discovery of another compound superconducting above the BCS temperature limit. The *iron pnictides*, which as a base have an iron atom Fe and a pnictogen N, P, or most importantly As, indeed raised much excitement since the discovery [4] of the compound LaOFeAs at least for the following reasons:

Chemical composition Pnictides belong to a layered transition-element-pnictide comprehensive material class with many possibilities of doping and chemical substitutions, offering important research potential while searching for higher T_c, or preparing HTS for commercial technologies.

Magnetism Their parent compounds are not insulators like cuprates but semi-metals; they contain an important concentration of magnetic Fe with a dominant role of the 3d orbitals near the Fermi energy, which raises the question of localization versus itinerancy of the electrons and is an opportunity to study the interplay between magnetism and superconductivity.

Renewal of the HTS research The appearance of a new HTS compound gives hope in solving the long lasting mystery of high temperature superconductivity, utilizing the accumulated experience of working with the cuprates. Most notably, strong electron correlations have not been observed by spectroscopy, which suggests that the utterly complex Mott physics of the cuprates may not be a necessary ingredient for high temperature superconductivity.

As a matter of fact, superconductivity in iron pnictides was discovered earlier in 2006 [5] with the compound LaFePO, but with a lower transition temperature $T_c \approx 4\,\mathrm{K}$, thus not raising the same excitement as the FeAs-based iron arsenides. Although they have a very similar structure to FeAs compounds, iron phosphides do not reach such high critical temperatures and their superconducting mechanism is believed to be different from iron pnictides [6].

1

Background - Iron pnictides

The iron pnictides being a very young research subject, there exist up to now little extensive reviews or material presenting the current state of research. Such reviews are confronted to a dilemma as already noted by Damascelli *et al.* in their 2003 cuprates review paper [7], but with good justification:

> *On the one hand it may be premature to proceed with an extensive review, but on the other hand it is helpful for the broader community to have access to a summary of the current state of the subject. It is our intention to present a* snapshot *of the investigation of the HTSCs by ARPES taken at the time of completion of this article. This will help the readers, especially those who are not photoemission experts, to sort through the extensive literature, learn about the outstanding problems, and become aware of the level of consensus.*

Now, history repeats itself and while cuprates research still has not reached any consensus, it is now the turn of FePn materials to serve as a "racefield" for new discoveries. The resulting new research field is in constant and very rapid evolution, where most subjects under study see the opposition of quite different results and scenarios.

Most such documents were published shortly after the discovery of pnictides. They typically present the different families, the structure of these compounds, their basic properties, and compare them to the cuprates [8]. Very recently though, a few papers attempt to depict the current state of research[1], still underlining many controversies and unsettled issues. Aswathy *et al.* published an overview of the pnictides [9] (June 2010) focusing on their synthesis methods and properties (structural, thermal, critical field and current density) rather than discussing the superconducting mechanism. Lumsden *et al.* made a synthesis of the studies on magnetism in the Fe-based superconductors [10] (April 2010).

[1] As time is passing at high speed in the scale of the pnictides research history, these may not be the most relevant at the time your are reading this thesis.

There is however one common characteristic of publications discussing the advance of the pnictides research: many seem to propose *intermediate pictures*, comprimising between different extremes that various experimental results seem to support. The strength of electron correlations is perhaps the subject presenting the most contrasted results, with on one side works supporting strong correlation approaches justified by proximity to a Mott insulating state [11, 12, 13, 14] (although no Mott state was ever detected in these materials), and on the other, theoretical works supporting weak [15, 16] to *moderate* electron correlations [17, 18] corresponding to itinerant electron states (see chapter 1.3.3), while recently being supported by experimental evidence [19]. On the theoretical side also, it is often emphasized that the superconducting properties, such as the gap symmetry, may depend very sensitively on parameters [20] or on details of the electronic structure [15, 21].

In this part some background knowledge of the iron pnictides is given in a *top-down* approach: first the basic properties of the pnictides are explained while presenting the different compound families, then several main current issues are presented in broad terms, and last the different theoretical models proposed for the pnictides are briefly discussed.

1.1 Iron pnictides families

It is instructive to start with a brief overview of the different pnictides families. All compounds share the basic characteristic of containing a two-dimensional FePn (Pn = As, P a pnictogen atom) layer with tetragonal structure at room temperature. There is an exception with the "11" *chalcogenides* family described below, the similar layered structure of which is only composed from FeSe[2]. The iron pnictides can mostly be classified in four groups with distinct crystal structures plus some composite compounds recently discovered which form their own category, as described below:

1111: RFeAsO, R a rare earth element (R = La, Ce, Pr, Nd, Sm, Gd, Tb, Dy ...) and AEFeAsF, AE a divalent metal (AE = Ca, Sr, Eu), RZrCuSiAs-type structure — family of the first discovered compound LaFeAs($O_{1-x}F_x$), with later the discovery of the analogue fluoride-arsenide series AEFeAsF. The parent compound is not superconducting but presents an antiferromagnetic transition at $T_N \approx 150\,\mathrm{K}$. By doping of the different ions (R, O or Fe), the compound becomes superconducting with the record of highest T_c among the pnictides and disputed between the following compounds: 55K for $SmFeAsO_{1-x}F_x$ [22], $SmFeAsO_{1-\delta}$ [23] and 56K for $Gd_{1-x}Th_xFeAsO$ [24] and $Ca_{1-x}Nd_xFeAsF$ [25].

122: AFe_2As_2, A an alkali metal (A = Ba, Sr, Ca, Eu ...): ThCr2Si2-type structure — this

[2]Strictly speaking, the term *iron-based superconductor* should be used when globally refering to the iron pnictides and the chalcogenides. However, for simplicity we will keep using the denomination iron pnictides in the rest of this thesis.

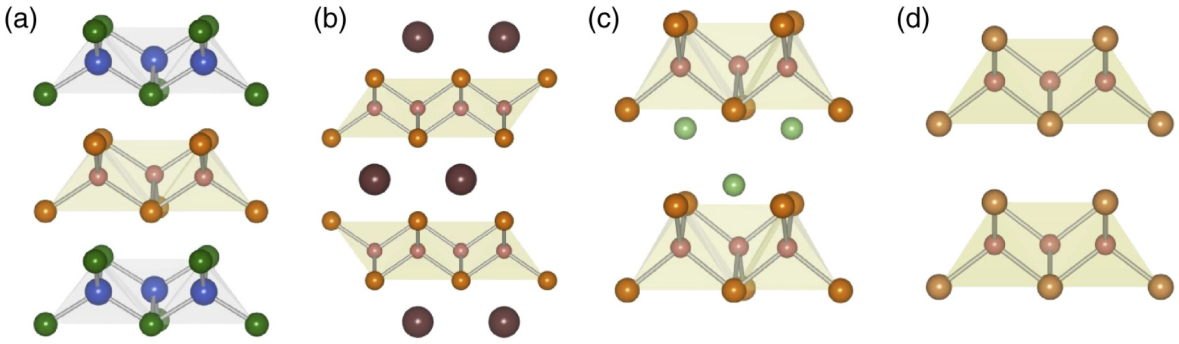

Figure 1.1: *Crystal structures of the 4 pnictides families:* **(a)** *LaFeAsO ("1111") ,* **(b)** *BaFe2As2 ("122"),* **(c)** *LiFeAs ("111"), and* **(d)** *FeSe ("11"). Figure reprinted from reference [8].*

compound is most reputed for its convenience in growing large single crystals[26]. It is for this reason probably the most studied among all compounds. The highest T_c found within family is 38 K in $Ba_{1-x}K_xFe_2As_2$ ($x = 0.4$).

111: LiFeAs, NaFeAs, Cu2Sb-type tetragonal structure — these two compounds present difficulties both in their synthesis and studies. Indeed, the highly reactive Li and Na ions evaporate during the high-temperature reaction synthesis process [27].
Exemplifying these difficulties is the fact that early studies have claimed the absence of structural or magnetic phase transition, both in LiFeAs and NaFeAs, but experiments on high quality NaFeAs samples have corrected this apparently curious properties by confirming the presence of both structural and magnetic transitions [27, 28], with the specificity that they occur at quite different temperatures, contrarily to the case of 122 compounds, at least in their parent state. 1111 compounds also present such a non-simultaneous transition, but it is experimentally harder to enquire [29]. Moreover, first principle calculations [30, 31, 32, 33] predict a stripe antiferromagnetic ground state for LiFeAs, which is left to be measured.
Similarly, superconductivity has been measured both in undoped Li and Na based compounds, but it is unclear whether superconductivity is possible in the stoechiometric compound, or needs deficiency of the Li/Na atom to appear. In particular, superconducting properties of LiFeAs have been found very sensitive to sample preparation [34, 35, 36].

11: FeSe, α-PbO-type structure — the simplest among the four structures, superconductivity is induced by deficiency of the Se atom or by doping of Te. A maximal $T_c \approx 15\,\mathrm{K}$ was found for the compound $FeSe_{0.5}Te_{0.5}$. This compound has attracted attention by the absence of As, and its simplest crystal structure among all compounds.

Composites: A last type not belonging to the 4 above families is the composite layered com-

pounds containing both antifluorite pnictide layers and perovskite oxide layers, such as Ti-doped $(Fe_2As_2)(Sr_3Sc_2O_5)$ ($T_c = 45\,K$), $(Fe_2P_2)(Sr_4Sc_2O_6)$ ($T_c = 17\,K$), $(Fe_2As_2)(Sr_4V_2O_6)$ ($T_c = 37.2\,K$), and Co-substituted $(Fe_2As_2)(Sr_4MgTi_{0.6})$ ($T_c = 26\,K$).

Our laboratory's research currently focuses on iron-based compounds, and has conducted research on several of these compounds. The compounds studied are mostly doped superconducting ones, as we focus on measuring the superconducting state properties of the pnictides.
In the 122 family, a systematic study of hole-doped $Ba_{1-x}K_xFe_2As_2$, electron-doped $BaFe_{2-x}Co_{2x}As_2$ with different dopings from underdoped to overdoped has been one of our leading research projects since 2009, focusing on nesting and geometry of the superconducting gap doping dependences. Other studied compounds include P-doped, Pt doped and Co-doped $BaFe_2As_2$ (Ba122), and P-doped Eu122.
In the 111 family, the LiFeAs compound was subject to measurement which underlined the very high sensitivity to sample preparation and sample homogeneity, as we observed a high unstability of results and large difficulties in reproducing measurements. NaFeAs compounds are one of the current subject of research, with the P-doped $NaFeAs_{1-x}P_x$ and Co-doped $NaFe_{1-x}Co_xAs$, mainly aiming at measuring the Fermi surface and superconducting gap geometry.
Another compound that was studied is $(Fe_2As_2)(Sr_4V_2O_6)$ (or $Sr_2VO_{3-\delta}FeAs$, thus labelled "21311") and is an example of the above composite compounds category.

1.2 Unresolved issues of the pnictides

In the course of my work, an important contribution has come from the inspiring weekly meetings discussing the research plans in the different projects in regard with the current advances of the pnictides research community. All the issues about this new family being naturally linked, it is useful to describe the different contential subjects around which revolve all pnictides studies today while trying to understand their fundamental superconducting mechanism.
A break down in several themes is proposed in an attempt to classify the existing research projects, and to discuss the issues with better clarity. However, links between the different subjects will often be made, as a totally independent treatment would be meaningless and bring too much repetitions.
The discussion will focus on ARPES results and the possible research prospects and different existing points of view besides our own opinions. At some occasions, reference to other probes are given. Comparisons will also be made with the cuprates, emphasizing the new behaviours observed with the pnictides and trying to interpret these differences. Basic concepts and phenomena will sometimes briefly be explained in order to allow understanding from a reader without much experience of the pnictides or HTS.

1.2.1 Superconducting gap symmetry

Seen as an important information to help deciding between competing theories, the superconducting energy gap is directly related to the energy required to break a Cooper pair and to the order parameter (OP) of the superconducting system. It can be most directly probed through ARPES measurements, basically appearing as a suppression of the electronic states at the Fermi level and the formation of a superconducting coherence peak at an energy defining the superconducting gap, which may possibly varying along the Fermi surface. Such gap observation represents a challenge as pnictides' energy gap values are considerably small, typically smaller than 10 meV, which also defines the limit of very high energy resolution in ARPES systems (see section 2.2.5 on resolution improvement works of our system).

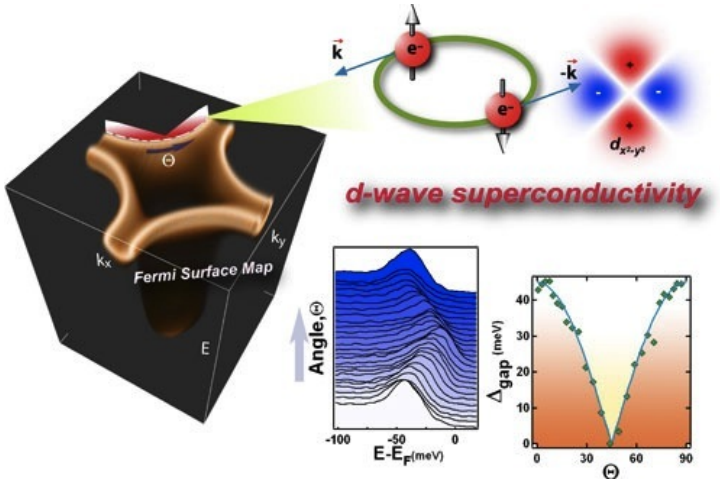

Figure 1.2: *d-wave gap for the cuprates.*

The gap amplitude can also be used to evaluate the coupling strength, through the ratio known from the BCS theory and according to the rule:

$$\frac{2\Delta}{k_{\mathrm{B}}T_{\mathrm{c}}} \gg 3.52 \quad \Longrightarrow \quad \text{Strong coupling regime} \tag{1.1}$$

where 3.52 is the BCS value. Larger ratio values obtained for the strong coupling regime high temperature superconductors (HTS) are typically around $7-8$.
In the cuprates, the gap has been shown (Figure 1.2) to have anisotropic "d-wave" symmetry. More precisely, it varies along the Fermi surface and becomes null in the (π,π) direction thereafter refered to as nodal direction. In the case of pnictides, the situation is quite different, starting with the Fermi surface topology. Several bands exist near the Fermi energy and may cross it under definite doping conditions [38]. Excluding the overdoped case, the consequence for the Fermi surface geometry is the presence of at least 2 hole-like FS "pockets" or sheets[3]

[3] This denomination depends on the consideration or not of the z-dependence of the Fermi surface.

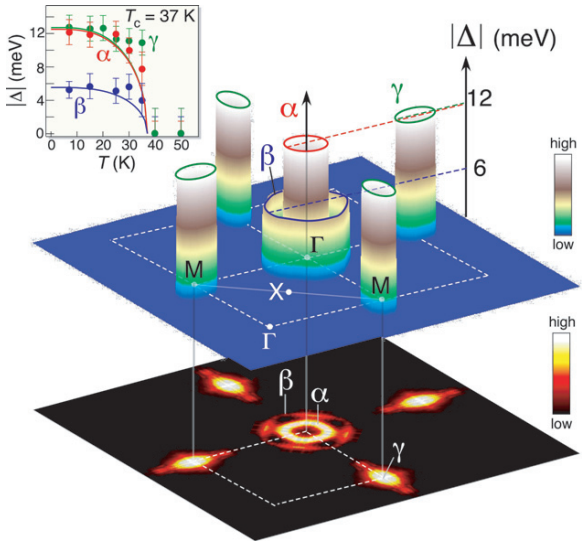

Figure 1.3: *Representation of the Fermi surface and corresponding gap for the sample* $Ba_{0.6}K_{0.4}Fe_2As_2$. *Figure reprinted from our work in reference [37].*

α, β at the Γ point, the BZ center with $k_x = k_y = 0$, and two electron-like pocket γ at the M point with a π rotational symmetry with respect to each other, for $\mathbf{k} = (\pm\pi, 0)$ or $(0, \pm\pi)$. An example of a measured FS is visible on the lower part of Figure 1.3. The corresponding gap symmetry along the different pockets is still under debate, with the following competing results and scenarios.

As one of our leading research work, ARPES results have been presented for the $Ba_{0.6}K_{0.4}Fe_2As_2$ compound of the 122 family, for which the gap has been shown to have different amplitudes on each pocket but to be isotropic along every FS sheets (see Figure 1.3): a larger gap $\Delta \sim 12$ meV on the inner hole FS and the electron FS, and a smaller one $\Delta \sim 6$ meV for the outer hole FS. Following this observation, the pnictides have thus been said to present *multigap superconductivity*. Two of the FS sheets, *nested* in the parent compound (connected by the $(\pi, 0)$ spin-density wave (SDW) vector), have a surprisingly close large gap value, which supports the importance of inter-band interactions for the pairing mechanism [37]. Besides, this seemingly s-wave gap is predicted to change sign between the hole and electron FS (opposite phase) [43], corresponding to an unusual $s_\pm$ pairing state with repulsive electron interaction at short range. The gap symmetry thus seems different from that of the cuprates. The major difference actually lies in the fact that scattering occurs between different FS pockets in the pnictides, while it occurs between two parts of the same FS pocket in the cuprates. Yet, as with the pnictides,

Indeed, recent works [39, 40, 41, 42] revealed a certain k_z-dependence of the Fermi surface, meaning the departure from the ideal two-dimensional electronic structure and thus representing an important difference between the pnictides and the cuprates. The three dimensionality of the electronic structure recently proved even more critical with the observation of a third hole band α' at the Z point, i.e. for $\mathbf{k} = (0, 0, \pm\pi)$ [42].

these two parts are connected by the antiferromagnetic (AF) wavevector. In the two cases, AF fluctuations thus seem to play a role, and the mechanism could be the same. Anyhow, the description of the process might be different.
While most seem to support this fully gapped, $s_{\pm}$ state scenario, other references based on com-

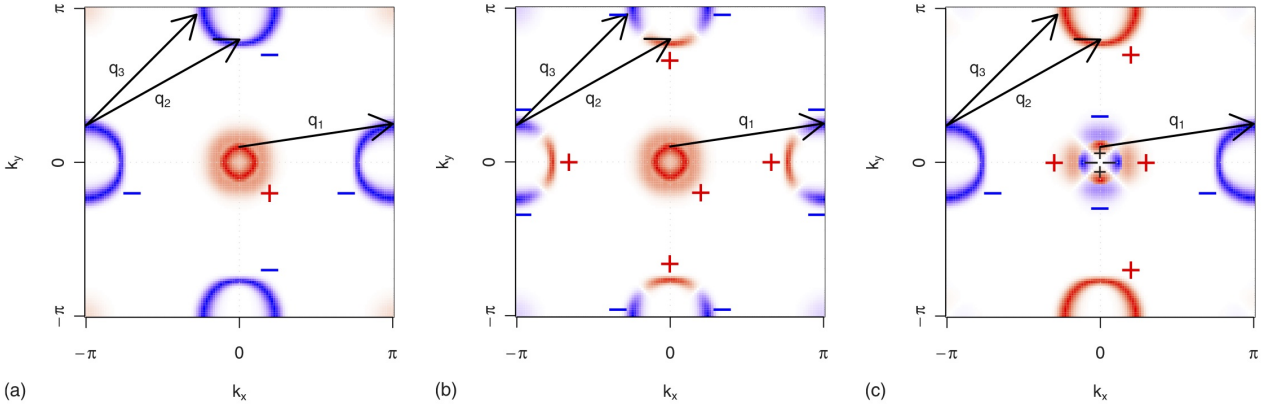

Figure 1.4: *Simulation of different pnictides gap symmetries for* **(a)** *the isotropic sign-switched s-wave,* **(b)** *the extended s-wave gap* $\Delta(\cos k_x + \cos k_y)$*, and* **(c)***, the d-wave gap* $\Delta(\cos k_x - \cos k_y)$*. The* q_i *arrows denote neutron scattering vectors. Figure reprinted from reference [45].*

putations [20] and penetration depth measurements [44] bring evidences for nodal gaps, which casts doubt about the $s_{\pm}$-wave orbital type. This further suggests the difficulty to express a universal gap function for the pnictides. Indeed computations have argued that the gap symmetry and its associate s-wave state may depend sensitively on parameters and variations in band structure, possibly leading to different symmetry ground state in different materials. In addition, Density Functional Theory (DFT) results suggest that contributions from surface could be the reason for ARPES results to observe only nodeless gaps [46]. Simulations of the different gap symmetries were made and are shown in Figure 1.4. It can be seen there that nodes on the electron FS sheets may still be compatible with a *s*-wave symmetry, with the so-called *extended s-wave gap*.
ARPES measurements, although insensitive to phase, can also give hints towards confirming this predicted scenario. The best method to study these symmetries is to have detailed mapping of the FS, and carefully observe the regions where nodes are expected (such as on Figure 1.4b). While excluding other symmetries than the general *s*-wave, observing gap would point towards the extended *s*-wave gap symmetry. This measurement has been performed by a member of our laboratory, in the hope of bringing the first experimental evidence for this scenario. A detailed study of the FS region potentially displaying nodes was performed (see section 3.1.2 for an overview of the experimental results). However, no evidence for the presence of nodes on the electron FS was found.

1.2.2 Fermi surface orbital character

The above section has discussed the symmetry of the order parameter along the Fermi surface as a critical information for characterising the superconducting state. The focus was put on the value of the gap in the different parts of the FS, which multi-pocket geometry as described in the previous section is now commonly accepted. However the complex FS geometry brings up the question of the orbital character of the different Fermi surface sheets. In particular, from all five Fe electronic 3d-orbitals having their importance for the electronic structure of the pnictides, it may be instructive to determine which orbital corresponds to which band and FS pocket. This may be used as additional information to confirm a specific electronic structure.

Experimentally speaking, the main tool to be used for studying the band orbital character is the different light polarizations in synchrotron facilities. Indeed, the different orbitals are polarization-dependent as a result of the selection rules imposed by the transition matrix elements (see section 2.1.3 for their derivation and section 3.2 for the description of the polarization-dependent experiment process).
On one hand, several experimental works attempt to figure out the details of the multiband structure of parent compounds using polarization-dependent results [47, 48]. Some give warnings about band structure measurements in doped superconducting samples [49]. Indeed, such measurements could bring falsed results at the M point where the electron-like Fermi surface may be gapped out, thus wrongly only displaying hole-like propeller-shaped FS pieces (due to a flat hole dispersion very near E_F) out of the four bands present there. On the other hand, some argue in favor of measuring superconducting samples [50], in which the complex phenomena of band splitting and folding from reconstruction below the usually simultaneous magnetic and structural temperatures T_N (T_S) are avoided, thus allowing a clearer observation of the sole selection rules effects on the bands.
Our position stands in the second group, as for instance our conclusions at the M point differ from the one by Yi *et al.* [49] mentioned before, indeed seeing the propeller-shaped as the normal occurance of the two folded electron Fermi surface sheets. We also support research of orbital character in the optimally doped compound $Ba_{0.6}K_{0.4}Fe_2As_2$, compound for which we have conducted the most thorough enquiry with the studies of superconducting gap discussed in the previous section, and of doping-dependence of the superconducting properties. For that compound, simulations of the selection rules effects over the whole Fermi surface are made, thus motivating the main experiment of this thesis on Fermi surface orbital character measurements of the precited compound.

Finally, discussions on the theoretical side often relate orbital and magnetism order, which is another motivation for performing these experiments. Indeed, several work attempt to describe and explain the magnetic properties [51], and minimal two orbital tight-binding models have been found sufficient to describe the magnetic state [52] whereas all five orbitals need to be considered to reproduce the band structure. This subject is approached in the next section.

1.2.3 Magnetism

Consecutively to the superconducting state gap and orbital character discussions above, one can look at a very important property shared by most compounds: the antiferromagnetic state. Indeed, in the phase diagram of many compounds, the AFM state occurs surprisingly close to the superconducting state. The main motivation of this discussion is to determine what role magnetism (spin fluctuations) holds in the pairing mechanism, or more generally of which nature and how important is the interplay between magnetism and superconductivity. Moreover, magnetic fluctuations can help to distinguish between different proposed gap symmetries.

For cuprates, the anti-ferromagnetic, Mott (charge transfer) insulator ground state is suitable for a Hubbard model description (strong coulomb correlations with localized magnetic magnetic moments). Anti-ferromagnetic fluctuations are visible in ARPES as "hot spots" of depleted intensity along the Fermi surface of a doped compound [53].
For iron pnictides, the ground state of the parent compound is not insulating but semi-metallic. Pnictides are seemingly itinerant systems [54] where magnetism arises from nesting-induced SDW type ordering. The pnictides enter this SDW ordered state below a critical transition temperature T_N, which moreover coincides to or is preceded by a structural transition at temperature T_S for the 122/11 and 1111/111 families respectively.
The nesting scenario, while being supported by most, has some competitors with for example the electronic reconstruction driven SDW [29]. This is motivated by the non-coincidence of the structural and magnetic transitions. Between these transitions, a progressive electronic structure reconstruction happens, meaning that both transitions may originate from global electronic structure reconstruction.
Electronic correlations thereby seem of quite different role and nature than in the cuprates, thus motivating further enquiries of the two families. Various works on theoretical and experimental grounds open new questions and scenarios based on the pnictides novel properties.

Muon spin rotation experiments [55] (μSR) on pnictides are supporting *soft magnetic fluctuations* (low energy spin fluctuations) emerging on doping away from an AFM or SDW state as key ingredients for superconductivity, rather than the preceding dominating cuprates scheme of strong electronic correlations in the vicinity of a Mott insulator transition.
Works on the theoretical side [56] propose a description using an *intermediate-to-strong* coupling picture, supporting *dualistic* itinerant-localized electronic states, where short-ranged frustrated spin correlations remains after the $\mathbf{q} = (\pi, 0)$ magnetic order is suppressed by doping. In that intermediate coupling picture, considering a metallic system so-called close to "Mottness" has shown good ability at capturing the T-dependences of spin-lattice relaxation rates measured by nuclear magnetic resonance (NMR). That work further supports the existence of *out-of-plane line nodes*, as spin-relaxation rates seem to indicate lines nodes in the gap, while most ARPES

results do not observe any in-plane node. This consideration of in/out-of-plane nodes seems to add an argument to the controversy of nodal (computations [20] and some experiments) versus nodeless (ARPES [37]) gap mentioned before, where the theoretical work proposed *disorder* or a *thermodynamical instability* of the $d_{x^2-y^2}$ state towards an s-wave state as an explanation to this apparent discrepancy.

In this regard, another current research ongoing in the group is a comprehensive study of the gap and its k_z dependence. Our belief is that the z-direction component of the gap $\Delta_z^i \sim t_\perp$ must be much smaller than the in-plane component. While considering a gap form of the type $\Delta^i \sim (\Delta_{ab}^i + \Delta_z^i \cos k_z) \cos k_x \cos k_y$, we expect that the z-term is too weak to bring about cancellation of the ab-term, and thus no node should be observed. This is consistent with the expectation of observed nodes solely due to the symmetry type, in this case the extended s-wave type.

1.2.4 Spin resonance and interrelation with superconductivity

A suggestion by Professor Ding let me study the subject of spin resonance in the HTS. A major question here is to determine which of the spin resonance phenomenon or superconductivity is causing the other. The spin resonance is naturally closely related to the magnetism questions discussed before, such as the itinerant electrons versus localized spins (or dualistic?) nature of the systems. Spin resonance from neutron scattering (NS) experiments appears as a magnetic excitations centered at a given wave-vector and has been seen strongly tied to the onset of superconductivity. Following are some results and interpretations made from NS spin resonance measurements.

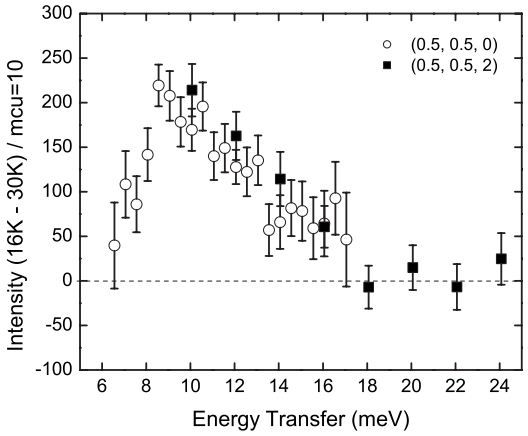

Figure 1.5: *Neutron scattering spin resonance peak seen in the difference between the inelastic-scattering intensities taken at temperatures 16K and 30K, at the momentum exchange* $\mathbf{Q} = (0.5, 0.5, 0)$ *and* $(0.5, 0.5, 2)$ *(from ref. [57]).*

Neutron scattering measurements at various momentum transfer are moreover predicted from computations [45] to be able to narrow the possible gap structure of pnictides. Indeed, NS resonances are predicted to occur specifically between parts of the FS with gaps of opposite sign. A specific transition (a certain wave-vector $\mathbf{q}$) can thus select scattering between certain regions of the Fermi surfaces, e.g. a given sheet or part of the FS, after what resonance may be observed on one or several types of gap ($s_{\pm}$, extended-s, $\mathrm{d}_{x^2-y^2}$). Here, ARPES providing the experimental maps for the FS surface could be used together with NS in order to verify this theoretical prediction.

Early results from experiments on the hole-doped compound $Ba_{0.6}K_{0.4}Fe_2As_2$ [58] showed a resonant excitation sharply peaked at momentum transfer Q, corresponding to the periodicity of the AFM order within each plane of iron spins in the parent compound $BaFe_2As_2$. Furthermore, the energy of this resonant excitation $\omega_0 \approx 14\,\mathrm{meV}$ taken together with the gap value $\Delta_0 \approx 12\mathrm{meV}$ gives a result for the scaling relation $\omega_0/2\Delta_0 \approx 0.58$ which is close to the value measured for a number of other compounds, ranging from 0.62 to 0.74. The temperature dependence of the resonant peak, falling down at zero precisely at T_c, seems to confirm the coupling of the excitation to the superconducting order parameter, while the cause/consequence order is still not defined. It also ensures the predominantly magnetic nature of the excitation. ARPES FS mapping together with these phase-sensitive results thus seem to corroborate the extended $s_{\pm}$-wave gap scenario discussed before.
In the case of electron-doped $BaFe_{1.84}Co_{0.16}As_2$ [57], the observed spin resonance is asymmetric in energy (see Figure 1.5), while it was apparently not for the hole-doped compound. Moreover, the spectrum is narrowed in the horizontal plane of the momentum transfer space, suggesting strong two-dimensional spin correlations. The spin correlations are associated with an enhancement of spin susceptibility $\chi''(Q,\omega)$ by exchange interactions, resulting in local spin polarisation. However, long-range static order is suppressed by spin fluctuations, thus giving an overall itinerant electron nature to the system. This contrasts with cuprates for which spins in the Mott insulator state are totally localized but develop some itinerant character through doping. Thus, non-trivial effects tend to make the two types more similar with doping.
Here, ARPES used together with NS may possibly give further support to a certain gap symmetry (because of the ability of NS resonance to show evidence for reversed-sign FS parts), or might shed light on the spin resonance phenomenon itself and its link with superconductivity.

1.3 Theoretical Models for HTS

During the course of the 9th *International conference on Spectroscopies on Novel Superconductors* (SNS 2010) in Shanghai last May, many theoretical models and concepts of the cuprates and pnictides were used and discussed, nourishing my desire to review some of these theoretical concepts. This research was also motivated by the necessity to relate several of our research

projects with theoretical models. Without getting into too much details, the coming part summarizes a theoretical approach for the pnictides.

1.3.1 The broad BCS picture

As a basic ingredient of superconductivity, the BCS picture "in the broad sense", namely the Cooper-pairing phenomenon, can be used while describing the band dispersion of the *Bogoliubov quasi-particle* (BQP, namely a linear combination of the particle and hole states which diagonalizes the BCS Hamiltonian). It is expressed as:

$$E_k = \sqrt{\varepsilon_k^2 + |\Delta(k)|^2} \tag{1.2}$$

where ε_k^2 is the dispersion in the normal state and $\Delta(k)$ is the superconducting gap and the BCS order parameter, which form is known for the cuprates as $\Delta_{\mathrm{d}_{x^2-y^2}}(k) = \Delta_0/2(\cos k_x - \cos k_y)$ but is still subject to debate for the pnictides. A consensus seems however to be coming out now with a s-wave gap of form: $\Delta_{\mathrm{s}_\pm}(k) = \Delta_0 \cos k_x \cos k_y$. The validity of the BQP picture can in principle be quantitatively checked by considering the *coherence factors*:

$$|u_k|^2 = 1 - |v_k|^2 = \frac{1}{2}(1 - \varepsilon_k/E_k), \tag{1.3}$$

and comparing them with their extracted values from the BCS spectral function:

$$A_{\mathrm{BCS}}(k,\omega) = \frac{1}{\pi}\left[\frac{|u_k|^2\Gamma}{(\omega - E_k)^2 + \Gamma^2} + \frac{|v_k|^2\Gamma}{(\omega + E_k)^2 + \Gamma^2}\right] \tag{1.4}$$

which consecutively appears in the equation for the ARPES spectra:

$$I(k,\omega) = I_0(k)[A_{\mathrm{BCS}}(k,\omega) + A_{\mathrm{inc}}(k,\omega)]f(\omega,T) \otimes R(\omega) \tag{1.5}$$

where $A_{\mathrm{inc}}(k,\omega)$ in an empirical function for the incoherent signal background, $f(\omega,T)$ the Fermi-Dirac function and $R(\omega)$ represents the experimental resolution.
However it is well known that the BCS theory all in all fails to describe the mechanism of high-temperature superconductivity, as the two major premisses of the theory are found invalid [59]. Firstly, pairing through phonon-electron interactions is insufficient to achieve pairing above the critical temperature $T \approx 30\,\mathrm{K}$. The second hitch of the BCS theory in describing HTS is that it is a mean-field theory, and consequently it ignores the local variations in the magnetic interaction that are believed to be important in the cuprates, and perhaps in the pnictides as well.

1.3.2 The localized electron picture

While looking for another source producing high temperature superconductivity, a magnon (magnetic fluctuations) based picture receives the support from probably the largest number of groups. A subsequent debate specific to the iron pnictides family is the nature of magnetism, and conversely the strength of electron-electron interactions. Indeed, as a major contrast with the cuprates, the parent state of the pnictides is not a Mott insulator, but a semi-metal seemingly presenting spin density wave (SDW), and is believed not to have correlations as strong as in cuprates. Correspondingly, different theoretical approaches have been proposed based either on a localized electron model or an itinerant system view (localized in k-space), with strong or negligible electron interactions respectively. These theories were largely developed already for the cuprates, and it should be reminded that although using two different points of view, they are basically equivalent. It was indeed shown that even in a case of a clearly localized electron system, an itinerant based method is still able to deliver sensible results, up to a certain degree of the correlation strength.

The localized models originate from the basic picture of an interacting electron gas in the tight binding model (localized wave functions around atom positions and restriction of their interactions with several nearest neighbours only), further neglecting the Coulomb interactions between electrons spans the *Hubbard model* which Hamiltonian is expressed (neglecting the hermitian conjugates terms) as:

$$\mathcal{H}_{\text{Hub}} = -\sum_{<ij>\sigma} t_{ij}\hat{c}^{\dagger}_{i\sigma}\hat{c}^{\dagger}_{j\sigma} + U\sum_{i} n_{i\uparrow}n_{i\downarrow} \tag{1.6}$$

The first negative term represents the kinetic energy. The second term, positive, represents the energy of double occupancy. From the Hubbard model, considering a single dominant hopping term and treating it as a perturbation to second order of perturbation theory, one can derive the *t-J model*:

$$\mathcal{H}_{t-J} = -t\sum_{<ij>\sigma} t_{ij}\hat{c}^{\dagger}_{i\sigma}\hat{c}^{\dagger}_{j\sigma} + J_{\text{eff}}\sum_{<ij>}\hat{\mathbf{S}}_i\hat{\mathbf{S}}_j \tag{1.7}$$

While many restrictions on the interaction range have brought this model, it can be generalized back by adding "higher order" correlation terms t, t', t''... etc, as well as other interaction terms such as electron-phonon interactions (e.g. with the *Holstein hamiltonian*), but also a pairing interaction term while modelling the superconducting state.
In the pnictides, the use of such models is justified by the assumption of a proximity of the normal state to a Mott transition, assumption which itself has been put to doubt and never proved by experiments. The recent evolution in the pnictides theoretical field rest for one thing on the more and more complex computations achieved within these models. From the simplest "two band model", works have gotten closer and closer to the full description of the electronic

structure, or the full consideration of the topology as predicted from the density functional theory (DFT) and the most advanced computations now treat up to five bands, which is the number we compute and currently observe on the Fermi surface: three hole bands around the Γ point and two electron bands around the M point. A different multiband approach is that of Eliashberg theory, based on the multiband Eliashberg equations, which was reported to reproduce the critical temperatures and gap values of various compounds of the 1111 and 122 families.

1.3.3 The itinerant electron picture

The itinerant electron approach appears natural for describing systems strongly believed to contain at least a certain part of itinerant magnetism, magnetic fluctuations being the most basic occurance of it. These methods rest on the fermiology nature of the pnictides as semimetals. One of the main tools of non localized methods is the *random phase approximation*, an infinite sum which as a useful result gives an expression for the effective spin susceptibility as:

$$\chi_q^{\alpha\beta}(\omega) = \chi_0^{\alpha\beta}(\omega) + \sum_{\gamma\epsilon} \chi_0^{\alpha\gamma}(\omega) J_q^{\gamma\epsilon} \chi_q^{\epsilon\beta}(\omega) \overset{\alpha=\beta=z}{\approx} \frac{\chi_0^{zz}}{1 - J_q \chi_0^{zz}} \tag{1.8}$$

where χ_0 is the Lindhart function, also known as the bare spin susceptibility, and the step is made using the Fourier transform coupling J_q. Further details on the use of the RPA can be found in reference [60].

Besides the different models we discussed, experiments also attempt to clarify the localized/itinerant electrons debate. In our case, the nesting picture we support puts emphasis on the inter-band scattering as an important mechanism in the pnictides superconductivity. The nesting is believed to be directly related to the antiferromagnetic fluctuations, which situates our view in the itinerant magnetism.

2

Angle resolved photoemission spectroscopy

Angle resolved photoemission spectroscopy met a great success in the studies of cuprates HTS, and has become a major tool in the studies of electronic excitations in these compounds. Several reasons motivated this fact:

Direct probing of single particule properties As a main reason, ARPES plays a most important role and is a powerful method because it is the most direct method to study the electronic structure of solids [7] (see section 2.1.3).

Improved resolution The years before and following the discovery of cuprates have also seen the great development of ARPES experimental tools, mainly with the introduction of the new generation of Scienta electron analyzers (see section 2.2.1).

Easy cleaving The cuprates' layered structure combined with a relatively important separation of the composing planes result in most of these compounds presenting a natural cleaving plane, some of them being particularly easy to cleave, like the Bi-based family of cuprates.

Quasi-2D electronic structure The layered crystal structure further results into a quasi two-dimensional electronic structure. Thus, the full resolution of ARPES in the plane is essentially sufficient to describe the whole structure of these materials while data analysis is made much simpler by the two-dimensionality.

Following over 20 years of research and techniques development with cuprates, it was but natural that with the emergence of a new type of high temperature superconductors, the iron pnictides, ARPES was going to be at the forefront of this new research. Indeed, most of the motivations above hold for the pnictides as well, however the results are found to be very different from the cuprates.

2.1 Theory

This part recalls the main theoretical aspects of the photoemission process, from the original *photoelectric effect* to the physics of ARPES, while pointing out the important assumptions and considerations supporting all further theoretical treatments.

2.1.1 Photoelectric effect

The *photoelectric effect* denotes the following original physical phenomenon on which are based all types of photoelectron spectroscopy experiments: an incoming beam of light is shined on the surface of a material, causing the emission of "photo"-electrons, provided that the electrons are excited to energies above the vacuum level (see Figure 2.1). The energy conservation observed in the process is expressed in the following way:

$$\hbar\omega = E_B + \Phi + E_{kin} \tag{2.1}$$

The energy of the incoming photon $\hbar\omega$ is transmitted to electrons which are bound to the material with energy E_B. They need an energy Φ (the work function) to escape the material with a final energy E_{kin}, as illustrated in Figure 2.1(b). The photoelectrons can be characterized by their kinetic energy and the xy-plane component of their momentum $\mathbf{p}_{\parallel}$, informations both measured by ARPES. Subsequently, the binding energy of the electron within the solid prior to excitation is obtained through equation 2.1, and its in-plane momentum is equal to that of the photoelectron by invariance of the problem in the xy-plane, and neglecting the momentum of the photon[1]. The electron dispersion relation $E_B(\mathbf{k})$ is thereby determined, corresponding to the ARPES experiment result in its simplest form.

2.1.2 Preliminary considerations

A few preliminary assumptions are usually made when considering theoretical treatments of the photoemission process.

Three-step model

A major challenge in the theoretical description of the photoemission process is the treatment of the solid-vacuum interface. One solution is to consider the *three-step model*, which as opposed to the more rigorous *one-step model* "artificially" decomposes the photoemission into three independent steps (see Figure 2.2):

[1]For a photon of energy 100 eV, the momentum is $\mathbf{k} = 2\pi/\lambda = E/\hbar c \approx 0.05$ Å^{-1}, which corresponds a few percents of the brillouin zone size in pnictides, comparable to the experimental resolution meaning that the photon momentum can be neglected below such energies, but should be considered when going to higher energies.

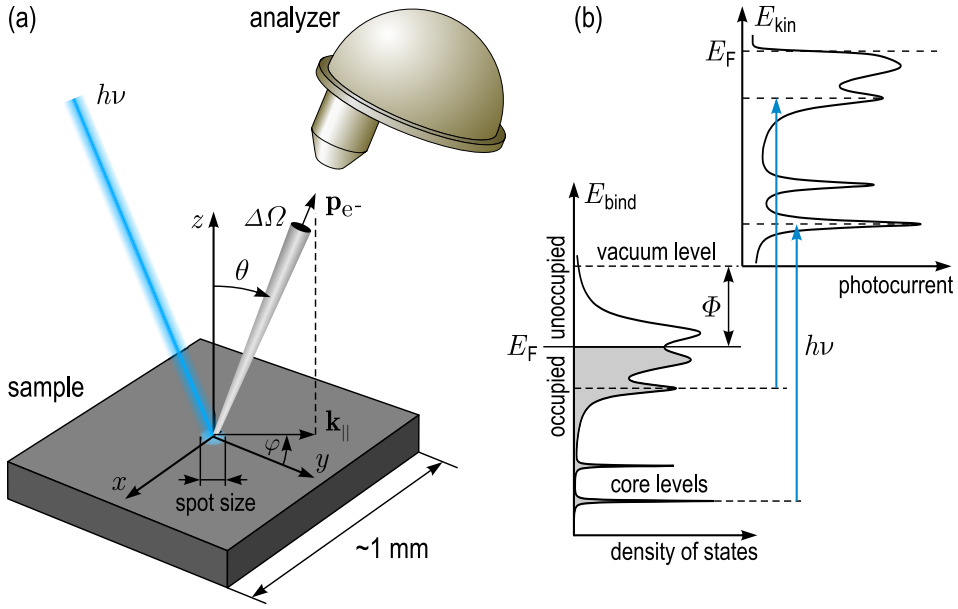

Figure 2.1: **(a)** *Sketch of an ARPES experiment. Photoelectrons with a given momentum* $\boldsymbol{p}_{e^-}$ *are detected by the analyzer.* **(b)** *Correspondence between measured photoelectron spectrum (above graph) and the corresponding original electron distribution in the solid. Two electron transitions are shown, denoted by the blue arrows. Figure reprinted from reference [60].*

1. Optical excitation of the electron in bulk.

2. Travelling of this electron to the surface.

3. Escaping of the electron through the surface into vacuum.

This allows us to only consider the state of the bulk crystal, omitting the surface and vacuum states, as our initial/final electron states $|\psi_i\rangle/|\psi_f\rangle$ are treated as independent. Two important points can be noted from the above simplified scheme. First, the transport of the electron to the surface should happen without any disturbance from the environment, in particular the electron should conserve its original energy and momentum, which means no inelastic scattering. This question is treated in a following point concerning *mean free path*. As discussed in the previous section, the interface-parallel component of the momentum is conserved in the third step.

Sudden approximation

The second fundamental approximation used in considering the photoemission process is the *sudden approximation*, which assumes an *instantaneous response* of the system to the photohole and *no interaction* with the escaping photoelectron. It mainly assumes that the dispersion of the outcoming electron basically corresponds to that in the material. The approximation is valid

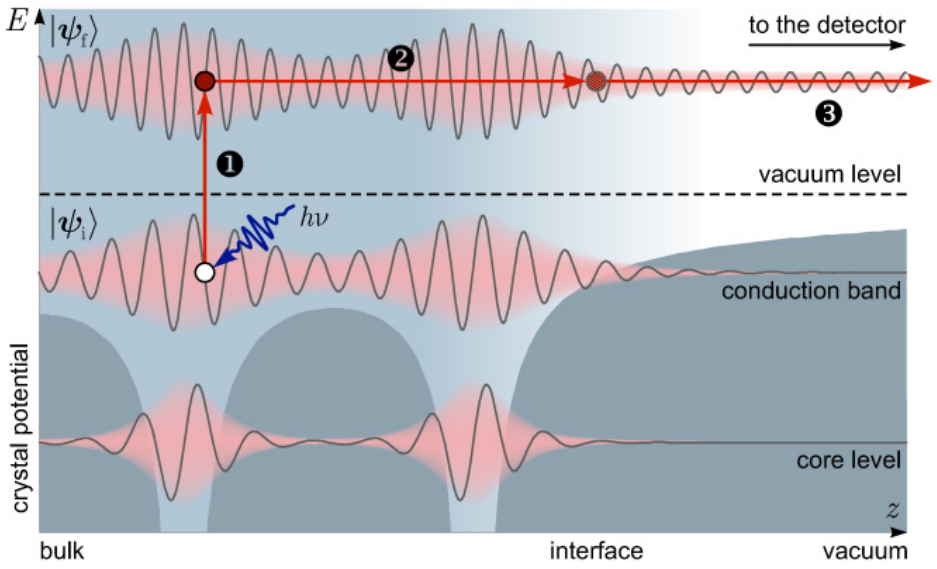

Figure 2.2: *Illustration of the three-step model.*

in the high-energy photoelectron limit, which corresponds to the situation of HTS [61].

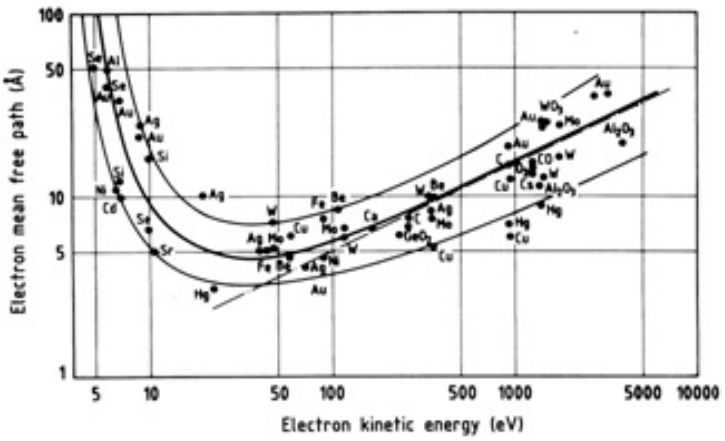

Figure 2.3: *Mean free path universal behaviour for different metals*

Mean free path

The *(electron) mean free path* denotes the average distance covered by an electron in a material between two scattering events. As proposed in a simplified view in the previous section, we expect excited electrons to travel through the material before escaping through the interface. The transport of electrons through solid matter follows a universal behaviour related to the electron energy. For the kinetic energy range of interest, from 10 to 100 eV, Figure 2.3 shows a

mean free path of only a few Angstroms. This subsequently shows:

- The surface-sensitivity of any electron spectroscopy method.
- The necessity to work with atomically clean, well-ordered surfaces and in order to probe the bulk properties of the material, and achieve UHV to preserve these systems.

2.1.3 Derivation of the photoemission intensity

Assuming the use of the three-step model, the photocurrent is related to the probability to undergo the three steps. The transport probability to the surface is described by the material mean free path. The probability of transmission through the interface depends on the electron energy and the work function of the material. The first step of electron excitation by the incoming photon thus only remains to be treated. It is briefly presented as in [61].

We consider an N-electron system, with initial and final states ψ_i, ψ_f. The measured photocurrent corresponds most generally to the sum of all possible transitions between the two states:

$$I(E,\hbar\omega) \propto \sum_{i,f} w_{if} \tag{2.2}$$

the transition probabilities w_{if} are obtained by the *Fermi's Golden Rule*, assuming a small perturbation Δ:

$$w \propto \frac{2\pi}{\hbar} \underbrace{\left|\langle\psi_f^N|\Delta|\psi_i^N\rangle\right|^2}_{\text{transition matrix elements}} \delta(E_f - E_i - \hbar\omega) \tag{2.3}$$

where the perturbation Δ is in our case the interaction of the electron with the photon electromagnetic field:

$$\Delta = -\frac{e}{2mc}(\mathbf{A}\cdot\mathbf{p} + \mathbf{p}\cdot\mathbf{A}) - e\phi + \frac{e^2}{mc^2}\mathbf{A}\cdot\mathbf{A} \tag{2.4}$$

$$\approx -\frac{e}{mc}(\mathbf{A}\cdot\mathbf{p} + \frac{1}{2}\mathrm{div}\mathbf{A}) \approx -\frac{e}{mc}\mathbf{A}\cdot\mathbf{p} \tag{2.5}$$

where in the first step we neglect a possible two photon process, choose an appropriate gauge and use the commutation relation. In the second step the divergence term is neglected using the *dipole approximation* for a vector potential $\mathbf{A}$ constant over atomic dimensions which holds in the ultraviolet region.
We can further isolate the transiting electron in the expression of ψ_i^N and ψ_f^N (using sudden approximation and assuming a single Slater determinant for ψ_i^N):

$$\psi_i^N = \mathcal{A}\phi_{i,k}\psi_{i,R}^k(N-1) \quad \text{and} \quad \psi_f^N = \mathcal{A}\phi_{f,E_{kin}}\psi_{f,R}^k(N-1)$$

where here k denotes a certain orbital and $\mathcal{A}$ is an antisymmetrization operator.
The next step usually introduces a trivial case — for example core-level photoemission or else

non-interacting electron system — followed by the derivation of the more complex general expression for (valence band) photoemission. The core-level/valence band approach is given now.

For core-level photoemission the remaining electrons final state can be in any of the excited state s of energy E_s by instantaneous relaxation, bringing:

$$\langle \psi_f^N | \Delta | \psi_i^N \rangle = \underbrace{\langle \phi_{f,E_{kin}} | \Delta | \phi_{i,k} \rangle}_{M_{f,i}^k} \sum_s \underbrace{\langle \psi_s^k (N-1) | \psi_{i,R}^k (N-1) \rangle}_{c_s} \tag{2.6}$$

with M_{if} the one-electron dipole matrix element, ${c_s}^2$ the probability that the removal of an electron from an orbital ϕ_k of the N-electron ground state leaves the system in the excited state s of the $N-1$-electrons system, or also an overlap matrix element. The zero or non-zero values of c_s depend whether the system under consideration is weakly or strongly correlated respectively. Therefore from eq. (2.2) we have:

$$I(\hbar\omega, E_{kin}) \propto \sum_{f,i}^{k} |M_{f,i}^k|^2 \sum_s |c_s|^2 \delta(E_{kin} + E_s - E_0 - \hbar\omega) \tag{2.7}$$

leading to core-level photoemission spectrum (sketched in Figure 2.4) with single lines corresponding to initial core-level, and their associate *satellites* reflecting internal excitations.

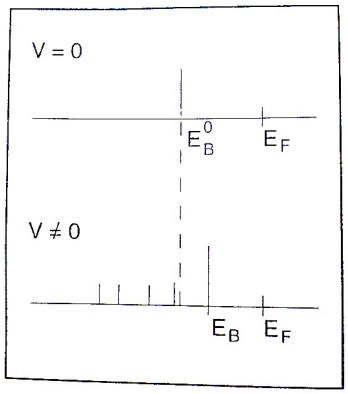

Figure 2.4: *Scheme of the core-level photoemission lines as modelized from a simple first order perturbation theory [61], with satellite lines in the case of a non-zero perturbation V.*

In reality, a smearing of the core-level peaks is observed, due to experimental resolution and mostly the presence of an inelastic-scattering continuous background (secondary electrons).

An important characteristic of the material can now be introduced, underlining its direct link with the photoemission experiment. For core-level photoemission, the *spectral function* is defined as follows:

$$A = \sum_s |c_s|^2 = \sum_s |\langle \psi_s^k | \psi_{i,R}^k \rangle|^2 \tag{2.8}$$

In metals, the outer electron system has a dynamical response to the core hole as follows and the spectral function has to be reexpressed:

$$g(t) = \langle i|f(t)\rangle \quad \text{where} \quad |f(t)\rangle = e^{-\frac{i}{\hbar}(H-E_0)t}|i\rangle$$
$$A(E) = \widetilde{g(t)} = \frac{1}{\pi}\Re\int_0^{+\infty} \mathrm{d}t\ e^{\frac{i}{\hbar}(E-E_B)t}g(t)$$

When studying HTS, the most important informations however are not in the core-level states, but in the states neighbouring the Fermi energy, which determine most physical properties of the material. For valence-state photoemission, wave-vector has to be taken into account in the transition probability (from delocalization of the electrons), we can note the following points:

- the periodicity of the Bloch function (as a basis for the crystal electron state) implies a momentum conservation that can be written as:

$$\delta(\mathbf{k}_{i||} - \mathbf{k}_{f||} + \mathbf{G}_{||})\ \delta(\mathbf{k}_i - \mathbf{k}_f + \mathbf{G})$$

- the imaginary part of the wave-vector perpendicular to the surface:

$$k_\perp = k_\perp^{(1)} + \mathrm{i}k_\perp^{(2)}$$

  accounts for the *electron damping*, resulting in a certain linewidth of the electron state Γ_e and a smearing of the momentum conservation. Contrarily to the component parallel to the interface, the perpendicular component does not follow a translation symmetry across the surface. As a result, the momentum perpendicular to the surface is not a good quantum number and approximations need to be used to get informations along that direction. It can also be probed experimentally by changing the incoming photon energy (see section 2.2.2).

For valence-state photoemission, the *one-particle spectral function* can be expressed in terms of the energy-momentum representation of the one-particle Green's function (using the Dirac identity):

$$A(\mathbf{k}, E) = \frac{1}{\pi}|G(\mathbf{k}, E)| \tag{2.9}$$

The *electron-electron correlations* induce necessary corrections to $A(\mathbf{k}, E)$ and $G(\mathbf{k}, E)$ which can be accounted for by adding the *self-energy* $\Sigma(\mathbf{k}, E)$ to the single-particle electron energy $E_0(\mathbf{k})$ leading to:

$$G(\mathbf{k}, E) = \frac{1}{E - E^0(\mathbf{k}) - \Sigma(\mathbf{k}, E)} \tag{2.10}$$

$$A(\mathbf{k}, E) = \frac{1}{\pi}\frac{\Im(\Sigma)}{(E - E^0(\mathbf{k}) - \Re(\Sigma))^2 + (\Im(\Sigma))^2} \tag{2.11}$$

more generally this expression justifies the *quasi-particle* picture of the electrons in an interacting-electrons system, where electrons are "dressed" with excitations due to various interactions: electron-electron, electron-phonon, electron-impurities, electron-magnons etc... The general meaning of the one electron spectral function norm is that of the probability of removing or adding a particle from the interacting many body system. Ideally, the self-energy can be probed experimentally with ARPES, as has been done for the cuprates. The real part is then related to the position of the bands, while the imaginary part is linked to the band broadness.
The complete equation for the photo-current from a crystalline solid thus follows from the previous equations:

$$I(E,\hbar\omega) \propto \sum_{i,f} \frac{\Im(\Sigma(\mathbf{k_i}))}{(E - E^0(\mathbf{k}) - \Re(\Sigma(\mathbf{k_i})))^2 + (\Im(\Sigma(\mathbf{k_i})))^2} \frac{\left|\tilde{M}_{i,f}\right|^2}{\left(k_{i\perp}^{(1)} + k_{f\perp}^{(1)}\right)^2 + \left(k_{f\perp}^{(1)}\right)^2}$$
$$\times \quad \delta(\mathbf{k}_{i||} - \mathbf{k}_{f||} + \mathbf{G}_{||})\ \delta(\mathbf{k}_i - \mathbf{k}_f + \mathbf{G})\delta(E^1(\mathbf{k}_f) - E^1(\mathbf{k}_i) - \hbar\omega + \phi) \cdot f(E,T)$$

In the above equation, we can note the following facts: the one-electron dipole matrix elements $M_{i,f} \sim f(\hbar\omega, \mathbf{k}, \hat{\mathbf{A}})$ contain complex physics and are difficult to resolve. In terms of actual experimental results, the matrix elements may induce quite non-trivial effects, typically resulting in the variation of the signal intensity while measuring the Fermi surface. Moreover, the presence of coherent and incoherent part of the spectral function results in the expectation of linewidths in our results.
A simpler expression is often used to synthetize the main elements of photoemission results:

$$I(\mathbf{k},\omega) = I_0 |M(\mathbf{k},\omega)|^2 f(\omega) A(\mathbf{k},\omega) \tag{2.12}$$

2.2 Experimental Setup

This section will present the technical setup of the ARPES experiment. As training during the project was taken mostly on the equipment of our Beijing IOP laboratory, but the main experiment data were obtained at the SLS synchrotron in Switzerland, the characteristics of both systems will be presented.

2.2.1 Scienta R4000 Electron spectrometer and experimental geometry

The Scienta R4000 electron spectrometer (analyzer), which is used at both IOP and SLS facilities, consists of a multi-element electrostatic input lens and a hemispherical deflector with entrance slits and a CCD camera detecting electron with resolution in two directions, corresponding to energy and momentum (see Figure 2.5a). The lens part modifies the kinetic energy of electrons received from the sample towards a given energy E_P, the pass energy, which is set by the voltage difference ΔV between the inner and outer hemisphere of radius R_1, R_2 respec-

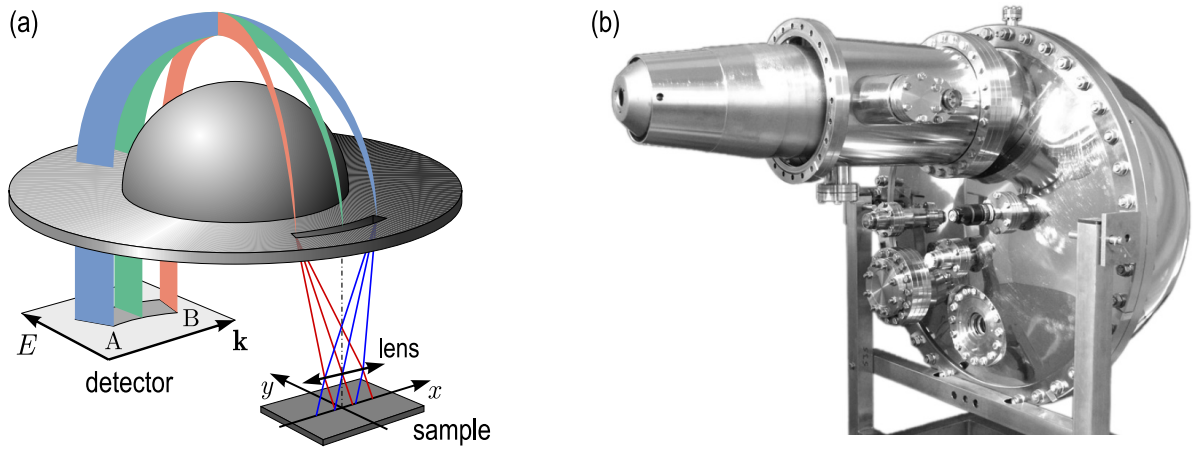

Figure 2.5: **(a)** *Scheme of the hemispherical deflector,* **(b)** *Picture of the Scienta R4000 analyzer.*

tively and according to the formula $E_P = e\Delta V/(R_1/R_2 - R_2/R_1)$ so as to obtain trajectories concentric with the hemispherical plates of the analyzer. Trajectories with smaller or larger curvature correspond to electrons with energy respectively slightly lower or higher than E_P. By further controlling the lens deceleration/acceleration in the so-called sweep mode, electrons can be resolved with large energy ranges. The second function of the lens part is to focus the electrons. In the angular-resolved mode[2], the electrons received from the sample with a certain acceptance angle — corresponding to the lens end opening nearest to the sample — are focused in order to reach the entrance slit at different positions depending on the direction of their initial momentum (see the 3 different coloured trajectories in Figure 2.5a).

The technical characteristics of the analyzer as found in [60] are summarized in Table 2.1. The energy resolution is directly linked to the pass energy E_P and the entrance slit width S

Acceptance angle	$\pm 15°$
Best angular resolution (FWHM)	$< 0.1°$
Best energy resolution	< 1 meV
Pass energies(angular mode)	$1 - 100$ eV
Minimal kinetic energy	0.2 eV
Minimal entrance slit	1 mm
Maximal resolving power	4000

Table 2.1: *Scienta R4000 analyzer characteristics.*

as in $\Delta E = E_P(S/R_0 + \alpha^2/4)$, with α the total acceptance angle (here $\alpha = 30°$) and $R_0 =$

[2]In contrast to the transmission mode where the electrons are not focused, i.e. the resulting resolution on the detector corresponds to the real space resolution, similarly to imaging devices. Besides, different angular-resolved modes exist: Ang30, Ang14 or Ang7, which allows to reduce the acceptance angle, in principle with a higher angular resolution, however it is in practice difficult to achieve.

$(R_1 + R_2)/2$ the mean radius. The electron signal intensity is however inversely proportional to E_P and S, which makes the control of these parameters a compromise between intensity and resolution. For high resolution measurement, we may thus choose a small slit and small pass energy. The second term shows that by reducing the acceptance angle, one should obtain a better resolution. The ideal (hardware) energy and momentum resolutions are moreover usually spoiled by imperfections of the optics, calibration, or various external factors. This part has been subject to many improvement works in our laboratory (see section 2.2.5). The resolving power of the analyzer is by definition the ratio of the pass energy to the energy resolution $R = E_P/\Delta E$.

It is useful to note in which regards this last generation of analyzers has brought major improvements to the angle-resolved photoemission experiment. The presence of a CCD camera with a direct energy and momentum resolution allows integration along many channels of a given energy in the sweep mode, largely improving the statistics and thus the resolution and data acquisition speed, while the large acceptance-angle[3] offers unprecedented band structure imaging and Fermi surface mapping.

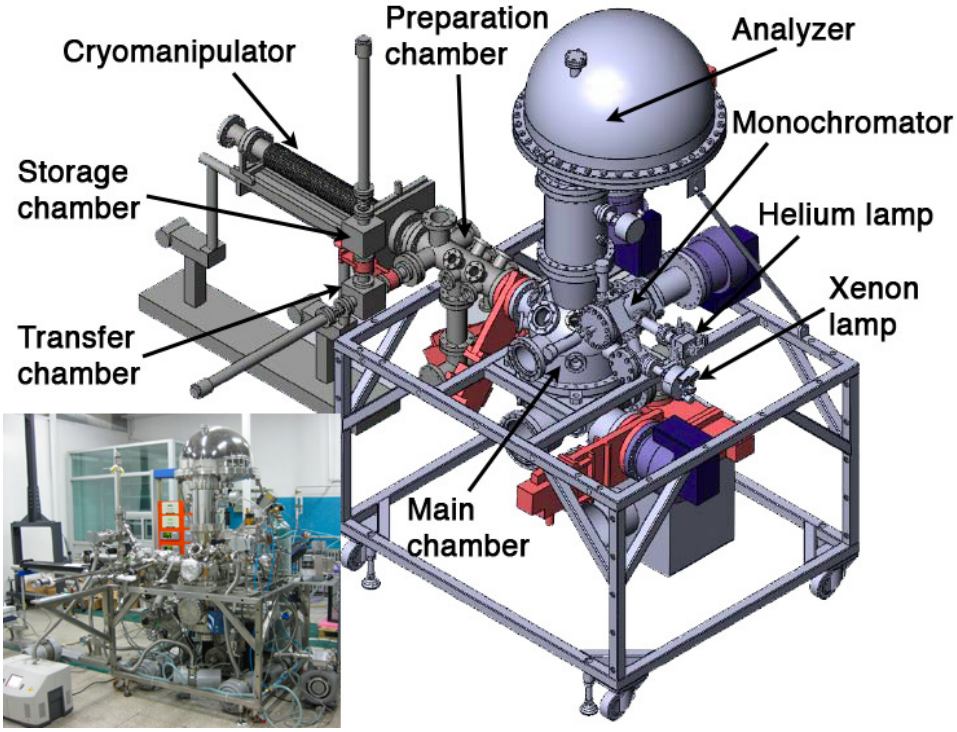

Figure 2.6: *Scheme of the EX7 laboratory ARPES system. The elements displayed in red colour are valves isolating the different chambers.*

The analyzer is connected to a main chamber with ultra-high vacuum of $P < 5 \cdot 10^{-11}$ Torr to prevent the sample surface contamination, itself connected to an ensemble of chambers isolated

[3]The latest analyzer model released in May 2010: the Scienta EW4000, allows an even larger 60° acceptance angle.

with valves in order to allow operation of the different parts safely and to preserve the quality of vacuum. Figure 2.6 shows the experimental setup at our EX7 laboratory, we do not show the SLS setup as it is in most regards similar to ours. The preparation chamber has tools for final sample preparation: evaporation of a gold layer on the surface of the sample holder for Fermi energy and resolution measurements, and cleaving of the sample. More details about the cryomanipulator are given in section 2.2.4.

2.2.2 Gas-discharge lamp light sources

The common ARPES laboratory setup is equipped with gas-discharge light as photon sources in the photoemission experiment. This is the case at EX7, where two lamps working with Helium or Xenon respectively are available.

The basic mechanism is similar for both lamps, although the design varies slightly according to

	He I	He II	Xe I	Xe II
Energy [eV]	21.218	40.814	8.437	9.570
Mean free path [Å]	≈ 10	≈ 5	≈ 25	≈ 20
Flux density [photons/s]	$0.8 \cdot 10^{13}$	$0.1 \cdot 10^{13}$	$> 10^{13}$	$> 10^{12}$
Spot diameter [mm]	≈ 2	≈ 2	≈ 2	≈ 2

Table 2.2: *Comparative characteristics of Helium and Xenon lamps for their most commonly used first and second orbital emission level (α lines). The mean free path is approximated from Figure 2.3. The flux density is only indicative as it depends on the gas pressure.*

the gas properties. A gas flux is created in a cavity at low vacuum $P \approx 4 \cdot 10^4$ mbar (for the best plasma stability), where a magnetic field is induced by surrounding magnets. The gas ionization is triggered by a sparkle from a high voltage source, after what the excitation/relaxation process is maintained by a microwave source. The plasma state is further enhanced and facilitated by the present magnetic field, which directs the "warm electrons" in spiral trajectories with a cyclotron frequency $\omega_c = eB/m \approx 10$ GHz for $B = 875$ Gauss. The relaxation of electrons from the lowest orbitals gives the light emission at specific energies.

Table 2.2 gives a comparison of both lamps' properties. The light orders correspond to emission from given orbitals. In order to select light from a given order, a so-called double-toroidal grating monochromator is used, which is a reflection grating combined with a beam focusing function. The two gratings are optimized for use with the different lamp, in energy range and orientation. A combination of mirrors, and finally a tube with narrow exit conduct the light towards the sample, where the light beam is given a 45° angle with the normal direction of the analyzer. The change in photon energies for the different lamps and orders selected have several implications:

k-range: The main concern is the link between the photon energy, and thus that of the corresponding excited electrons, and their momentum, as given by $E = \hbar^2\mathbf{k}^2/2m$. More

precisely, for a given energy E the range of observable in-plane momentum $k_\parallel$ is limited as of $k_\parallel \leq \frac{\sqrt{2mE}}{\hbar} \sin\frac{\alpha}{2}$. Therefore, the higher the photon energy, the larger the k-range in angular mode. However, the k-resolution also decreases in consequence.

k_z variation: For a fixed $k_\parallel$, a change in photon energy implies a change in the k_z momentum component. This is of importance for materials with three-dimensional electronic structures, which is the case for pnictides as discussed in footnote 3 (page 10). Through empirical determination, the following "photon energy – k_z" correspondence was found for pnictides: $E_{k_z=0} \approx 21, 45, 80\,\text{eV}$, $E_{k_z=\pi} \approx 32, 60\,\text{eV}$ (where $k_z = 0, \pi$ stands for $k_z = 2n\pi/c, (2n+1)\pi/c$ and will be used in the rest of this thesis).

Change in flux density: For a given lamp, usually the first order is the strongest, and intensity is considerably reduced for the next orders. The second order is still usable with a flux density half than the first order or less.

The k-range limitation is one of the drawbacks of using lamp sources. Typically for the pnictides, the chosen light is that of He I, because it has relatively high intensity and its energy happens to correspond to $k_z = 0$. In this case, the k-range is limited to about half of the first BZ size, which explains the "narrow" mapping range obtained in laboratories. Another drawback is the quite large spot size (larger than a typical sample size), which gives a limitation in angular resolution. An advantage is the higher energy resolution one should achieve with these settings, close to the theoretical resolution.

2.2.3 Synchrotron light sources

The demanding light intensity and focus requirements in ARPES can be well satisfied with light from synchrotron sources. Without entering too much details, the aspects related to the ARPES experiment are briefly presented.

Synchrotron light originate from the fact that a high energy charged particle submitted to an acceleration normal to its trajectory emits electro-magnetic radiation in the UV to X-ray range. The task is performed by a magnetic undulator placed at a beamline — a segment placed tangent to the accelerator ring — allowing to select light with energies in the range $10 - 800\,\text{eV}$ and with specific polarizations: circular positive/negative (C+/-), linear horizontal (LH) and linear vertical (LV). Light from different polarizations have energy limitations as follow: $E_{\text{C}\pm} \in [50, 800]\,\text{eV}$, $E_{\text{LH}} \in [10, 800]\,\text{eV}$ and $E_{\text{LV}} \in [100, 800]\,\text{eV}$. The resulting light has highest intensity at a given energy (the fundamental mode), and is further monochromatized by a plane grating monochromator and focused by an ensemble of mirrors.

The characteristics of the SLS synchrotron and beamline are given in Table 2.3. The advantages of synchrotron source are multiple: high intensity, variable energy and polarization, large k-range covered for high energies.

Energy range (polarization dependant)	$10 - 800\,\text{eV}$
Beam spot size	$50 \times 100\,\mu\text{m}$
Resolving power	10^4

Table 2.3: *SLS synchrotron and SIS X09LA beamline characteristics.*

2.2.4 Cryomanipulator and sample preparation

In order to probe different portions of k-space, further than just a "slice" visible from the intrinsic range of the analyzer, the sample is set on a manipulator with a certain number of degrees of freedom. The manipulator is combined with a cryostat and a temperature controller, which using a flux of liquid helium allows cooling down towards 10 K.

EX7 laboratory manipulator: our laboratory manipulator only has one degree of freedom φ. Figure 2.7 (right) gives a representation of the single rotation in real-space, around the axis of the manipulator, also around the "axis" formed by the slit direction. In k-space, this corresponds to a translation in a direction perpendicular to the slice obtained from the analyzer intrinsic angular range.

SIS X09LA beamline manipulator: this manipulator has three degree of freedom for a complete probing capacity of the k-space. Figure 2.7 (left) shows the real-space three rotation directions. In terms of k-space, the *Tilt* angle corresponds to the φ angle above. θ provides a translation along the slice direction, and ϕ rotates the slice in k-space.

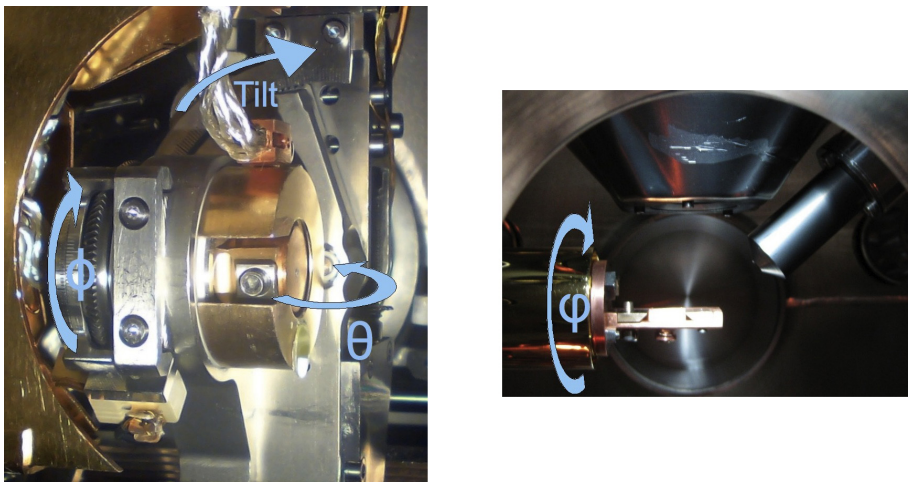

Figure 2.7: *(Left) picture of the X09LA manipulator with 3 angles of rotation, (Right) picture of the EX7 manipulator with a single angle of rotation.*

The sample preparation is a critical step of the whole experiment. Indeed, the quality of photoemission data depends very sensitively on the surface quality, which in turns requires of course a good sample quality but also a good cleave. Samples should thus be prepared with the highest care. The preparation process starts with the choice of a good piece of crystal among a

batch, which means a homogeneous piece with a crystal plane as a surface, visible from its shiny appearance. It is chosen or cut with size $1 \times 1\,\mathrm{mm}$, and thickness $\approx 0.1 - 0.2\,\mathrm{mm}$. The piece of crystal is glued on a sample holder with a small quantity of epoxy or ideally with conductive silver paste[4]. Secondly, a metal tip should be prepared to be fitted onto the sample, the tip head being crafted with a slightly smaller size than the crystal size. Once the crystal has stuck well on the surface (after $\approx 30\,\mathrm{min}$ heating at $T \approx 100°\mathrm{C}$), the tip is glued onto the sample again with a little amount of the chosen product (see Figure 2.8).
The prepared sample is transfered to the preparation chamber for cleaving, which is done after

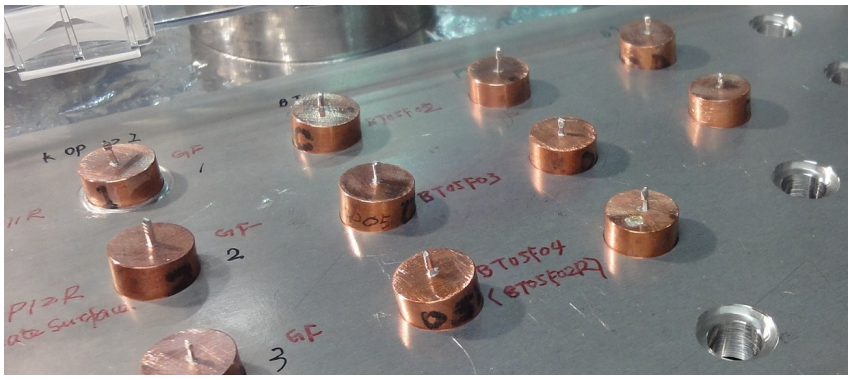

Figure 2.8: *Array of prepared samples with the X09LA holder type.*

cooling down to the lowest possible temperature ($T \approx 10\,\mathrm{K}$) by kicking off the tip with another stick. Usually, at least part of the sample is cleaved in a clean way, but the best is to obtain a full cleave resulting in a shiny mirror surface, otherwise inhomogeneity can bring complications when measuring different parts of the sample.

2.2.5 Technical and calibration work

In the course of the project, much time was spent on improving the performance of our equipment. In particular, the energy resolution ΔE is a critical parameter for ARPES, especially in laboratory conditions (use of lamp light source), where focus is put on ultra-high energy resolution, for example measuring the superconducting gap[5] rather than doing Fermi surface mapping better performed at synchrotron ARPES facilities. This part will give an overview of the techniques which were used, such as the baking process. It will also discuss the issues that were met and the way they were successively solved. The overall motivation was the improvement of the energy resolution, which at the beginning of this work did not get below 10 meV in the finest

[4]If choosing insulating glue, one can spread a layer of graphite spray to put the sample and holder in electrical contact, and prevent charging of the glue by electron emission. The use of silver epoxy has however proved more efficient. While being less strong than other glues, it is strong enough for pnictides compounds, in general all cleaving easily.

[5]In principle, a resolution ΔE is able to detect a gap of size $\Delta_{\mathrm{SC}} = \Delta E/2$.

settings, and has been most recently improved towards $\approx 2.5\,\text{meV}$ (end of July).

Baking process After modifying the experimental setup, or repairing certain parts, the vacuum chambers that have been vented and opened require baking. The main purpose of the baking process is to get rid of water-like residuals on the walls of the chamber by evaporating them. A first layer of aluminium is applied on the equipment, followed by

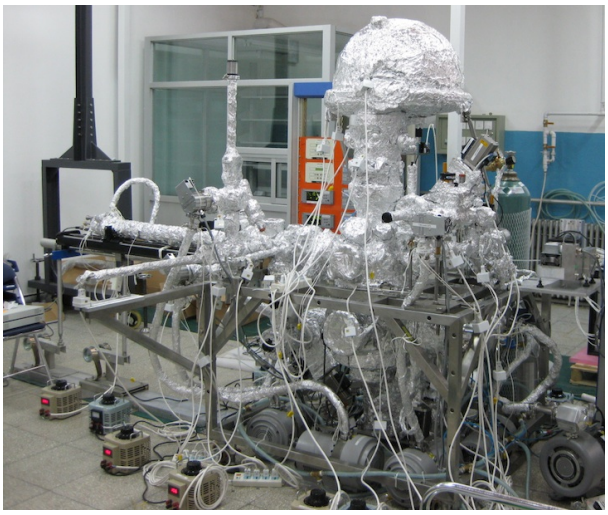

Figure 2.9: *Equipment covered with aluminium during the baking process.*

resistance-heating bands and finally a second layer of aluminium (see Figure 2.9). The aluminium can both protect the pieces and diffuse heat. Voltage transformers are used to control the power transmitted to the heating bands, and thus the temperature which is checked by probes set in different parts of the equipment. The equipment is then heated to a temperature $T \approx 80 - 100°\text{C}$, and set for pumping for 2 to several days. At high temperature the pressure will typically go down to $10^{-9}\,\text{mbar}$, and only after cooling down will the pressure reach values $\leq 5 \cdot 10^{-11}\,\text{mbar}$.

Replacement of the light tube and correction of the light filter position

These two problems originated from a design incoherence of pieces bought from different companies: the tube transmitting the light from the grating to the main chamber and the analyzer lense. The tube orientation could not be adjusted to direct the light beam to the middle point with regard to the analyzer lense. A first test with a newly designed, thinner tube did not bring significant improvement (see Figure 2.10) with even a slightly worse resolution for the case $E_p = 2\,\text{eV}$ and an overall worse stability over the angular range. The best resolution we achieved then was $\Delta E \approx 5$, which was about $2 - 3\,\text{meV}$ worse than the system at Tohoku University, thus not yet satisying. We subsequently made several tests, until the problem was identified as originating from the bad quality of the graphite spray

applied on the tube[6]. After applying a high quality graphite to our tube, the resolution was significantly improved.

Besides this problem, an error in the initial mounting resulted in the unefficient position

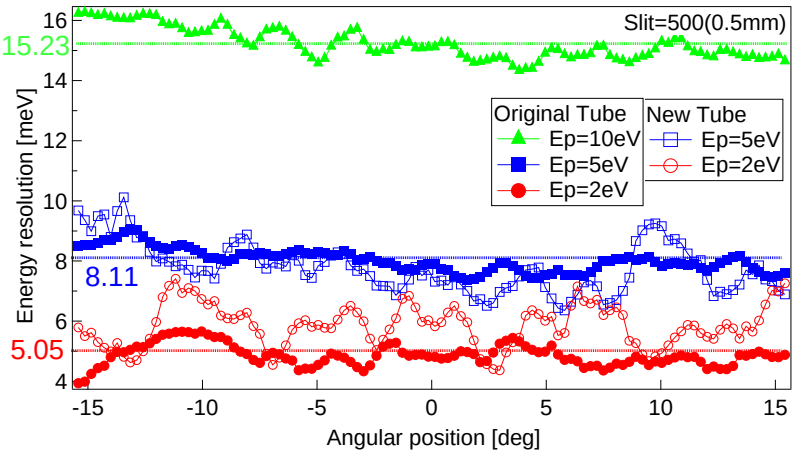

Figure 2.10: *Results of resolution determination on a gold surface before and after changing the lamp tube. The x-axis corresponds to different channels of the analyzer and the y-axis the corresponding ΔE. The curves of different colors (different markers) correspond to different pass energies E_p, while the filled (empty) symbols correspond to the results for the original (new) tube respectively. Figure made by Xiaoping Wang.*

of the light filter, a membrane transparent to the UV light from the Helium lamp. That filter was placed too far from the light source, which resulted in a large intensity loss as the small diameter of the transmitting membrane only lets the central part of the beam through. This problem was simply solved by inverting the position of that filter and the valve separating the Helium lamp from the gratings chamber.

These modifications required the dismantling of a whole part of the apparatus, and its re-mounting, giving a good opportunity to get more familiar with all the constituents of our system, including the Helium lamp, the Xenon lamp, their associate pumps and cooling system, the gratings and the lamp tube. It also gave me an active formation on the baking process of the high vacuum apparatus, as described above.

Remnant magnetic field in the main chamber While carrying out the different lamp tubes tests, a non-negligible magnetic field of about 10 mGauss was detected in the main chamber. One should avoid any remnant magnetic field there as this could lower the momentum resolution. We thus conducted a careful inquiry of the magnetic field geometry all around

[6]This layer of graphite applied on the tube lamp but also on the lense head has the purpose to avoid electro-magnetic field perturbation between the different parts which can be charged as a result of the photoemission process.

the inner space of the chamber, and the influence of the original and the new lamp tubes. We suspected different elements as possible sources of this magnetic field: the analyzer, the main chamber ion pump and the lamp tube. The measurement showed that the analyzer was the main source of the perturbation magnetic field. For now, we are coping with this remnant magnetic field.

Gas leak detection While carrying out resolution measurements, we encountered a problem with the lamp, where certain light orders seemed to have disappeared. The reason turned out to be a leak in our vacuum chamber with a contamination of the Helium gas from the lamp. Locating the gas leak is a delicate problem but can be done using a special Helium gas detector which allows to probe the Helium flux once connected to the main chamber pump. By releasing a little bit of Helium gas at specific positions outside the chamber, the position of the leak can be detected.

Checking the cryomanipulator thermal and electrical connections Our temperature control device was suspected to show unreliable temperature informations, and the 4-points measurements at the sample position's electrical connections were checked as being one possible source spoiling the resolution. The grounding also needed to be checked. Engineers from *VG Scienta* came in early May to assist us in these check-up, both thermal and electrical connections then appeared to be working fine. However, a later test seemed to show the influence of the temperature control device. Namely resolution systematically improved by $1 - 2\,\text{meV}$ when turning off the device. As this probably meant a current leak into the manipulator and sample support, the cryomanipulator was unmounted, the connections were remade and a broken temperature probe was replaced.

After a later test in June of the analyzer performance with a gas cell providing emission of electrons with very precise single energy, it was concluded that the analyzer worked perfectly, but that our manipulator design still had some flaws. In particular, the plug and connection between the manipulator and the temperature controller were found to be the main source of the resolution problem with a high sensitivity to external signals. After carefully insulating this connection, the resolution was finally improved to 2.5 meV, close to the theoretical limit.

3

Experimental work

This section presents the experimental results obtained from three different facilities: our own equipment at the EX7 IOP laboratory, Professor Takahashi's ARPES laboratory at Tohoku university and the SIS beamline at the Swiss Light Source (SLS). First, a few simple analyses are made on results with two novel pnictide compounds, after what the results of my own research on orbital characterization are presented.

3.1 Data analysis of two novel compounds

Prior to the main results of this thesis, some analyses will be presented on two novel compounds, for which I assisted Xiaoping Wang and Tian Qian in measuring at our laboratory, with a later measurement solely made by Tian Qian in Tohoku University. We purposedly start with typical description of results, in order to progressively develop a better insight for the results of my own experiments presented in section 3.2.

Measurements are made on our equipment as described previously in section 2.2 and very similar ARPES facilities at Tohoku University. One experiment typically requires 4 to 5 days for obtaining the different type of results, which are usually divided in the two following steps: mapping of the Fermi surface, then high resolution measurements of the gap and/or of the band structure along high-symmetry directions of the Brillouin zone (taking cuts between Γ, M and X points).

3.1.1 Band structure and Fermi surface of $BaFe_{1.9}Pt_{0.1}As_2$

This sample has been provided by Haihu Wen from a collaborating laboratory of the institute. It is a new compound belonging to the 122-family where Pt is used as electron-dopant, Our optimally doped samples have $T_c = 25$K.

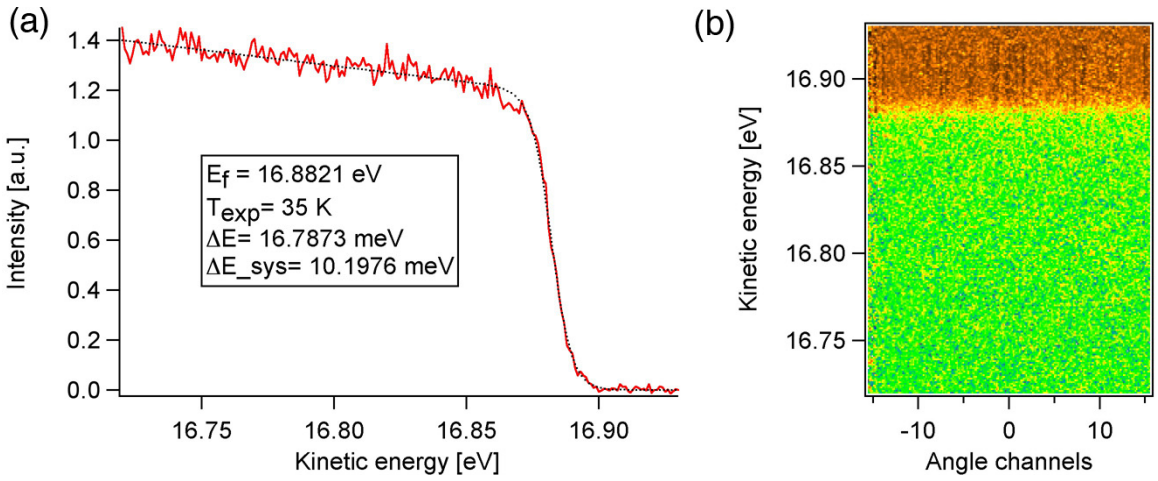

Figure 3.1: *Determination of the Fermi energy and the energy resolution at $T = 35\,K$, $E_P = 2\,eV$ and Slit 400.* **(a)** *Red curve: Integrated signal intensity near the Fermi level, black dotted curve: fitted Fermi-dirac function.* **(b)** *gold intensity spectrum along the different channels of the analyzer in the Ang30 mode, with "all range" normalization.*

A necessary step in any ARPES experiment is the determination of the Fermi energy E_F and the energy resolution ΔE. The sample being in electrical contact with the copper holder, the Fermi energy can be determined by measuring the photoemission signal of the neighbouring surface, where a gold layer was deposited (another possibility is to clean the copper surface by sputtering, for example with an argon gun). The gold or copper photoemission signal near the Fermi level ressembles a Fermi step (see Figure 3.1), with a certain linewidth determined by a combination of the temperature and the overall resolution. By deconvoluting the intrinsic thermal broadening from the overall broadening, we determine the system resolution as the energy width corresponding to a 90 to 10% of the step size[1]. In this case choosing high resolution parameters, we find a Fermi energy $E_F = 16.882\,\mathrm{eV}$ and a resolution $\Delta E = 10.2\,\mathrm{meV}$. As the resolution typically varies with pass energy and slit size, the process above is repeated using the different parameters that may be used in the experiment.

Figure 3.2 shows the result of Fermi surface mapping for 2 samples from the same batch successively measured. The mapping, characteristic of ARPES, is achieved by measuring successive "vertical slices" while varying the orientation of the sample, in this case the φ angle along the manipulator axis. A resolution of 10-30 meV is usually sufficient to reveal the Fermi surface of pnictides. We thus use slit 600 and $E_P = 10\,\mathrm{eV}$. As expected for the Fermi surface of Fe pnictides, the obtained result consists in two pockets located at the Γ and M points. The results correspond to an "energy-cut" at E_F (integrating the spectra within $\pm$2meV with respect to E_F) in the 3D $k_x - k_y - E$ intensity matrix obtained as a result of mapping.

[1]The energy resolution is thus subject to ambiguity between different groups, choosing different percentage of the step size to define the resolution. Our definition from 90 to 10% is a quite demanding one.

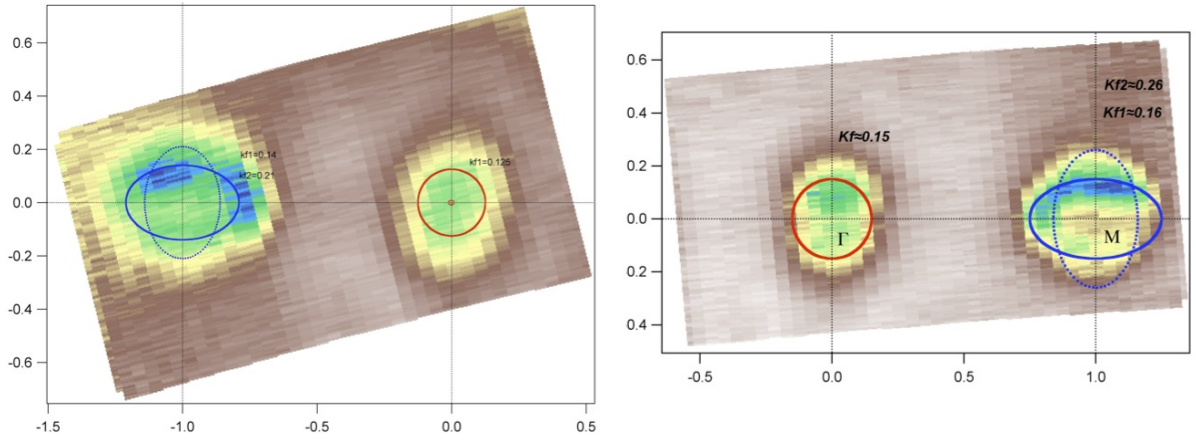

Figure 3.2: *Fermi surface mapping for two $BaFe_{1.9}Pt_{0.1}As_2$ samples, measured at 30K, with resolution $\Delta E \approx 20meV$.*

The mapping scope is chosen to focus on measuring the Γ and M points, and could be extended by symmetry to draw the whole first Brillouin Zone because of the 4-fold symmetry of the crystal, although actual measurements show variation of the intensity pattern at the different M points for $\mathbf{k} = (0, \pm\pi), (\pm\pi, 0)$. In our case, the angle-range covered on the θ orientation is $\pm 15°$. The corresponding area covered in the k-space is further determined by the incoming electron energy, from the simple relation $k = \sqrt{2mE/\hbar}$. With the absence of a Laue camera for crystal orientation, the approximate measurement direction $\Gamma - M$ is achieved by placing the sample with 45 degree with regard to the a or b direction, usually visible from the shape of the single crystal.
The red and blue lines respectively drawing a circle at the Γ point and two ellipses at the M point correspond to the k_{F} points. It is extracted from the intensity versus energy and momentum plots, i.e. slices in Figure 3.2, and along a symmetry direction as shown with the dotted-lines at $k_x = 0, \pm 1$, respectively crossing the Γ and M points. The extraction method is shown in Figure 3.3, with the vertical blue lines corresponding to the position of k_{F} and the circles on Figure 3.2.

In a second part, we use the information of the mapping, specifically the angular (or k) position of the Γ and M points to carry out high resolution measurements at these two points. Figure 3.4 shows some of these measurements together with a technical artifact: the second derivatives of the plots. Here we give the second derivatives with respect to energy and momentum, which are defined respectively as: $\frac{\partial^2}{\partial E^2} I(E,k)$ and $\frac{\partial^2}{\partial k^2} I(E,k)$. The second derivatives allow a clearer view of the bands. We can now confirm the nature of the Fermi surface pockets observed before. At the Γ point, two bands of hole type are visible, the outer band reaches E_{F}

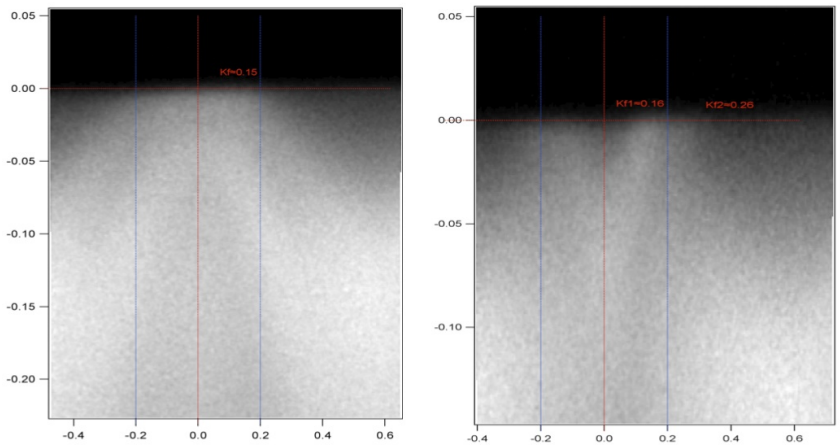

Figure 3.3: *Determination of the k_F vector around: the Γ point on the left, the M point on the right. The position of k_F is where the band reaches E_F .*

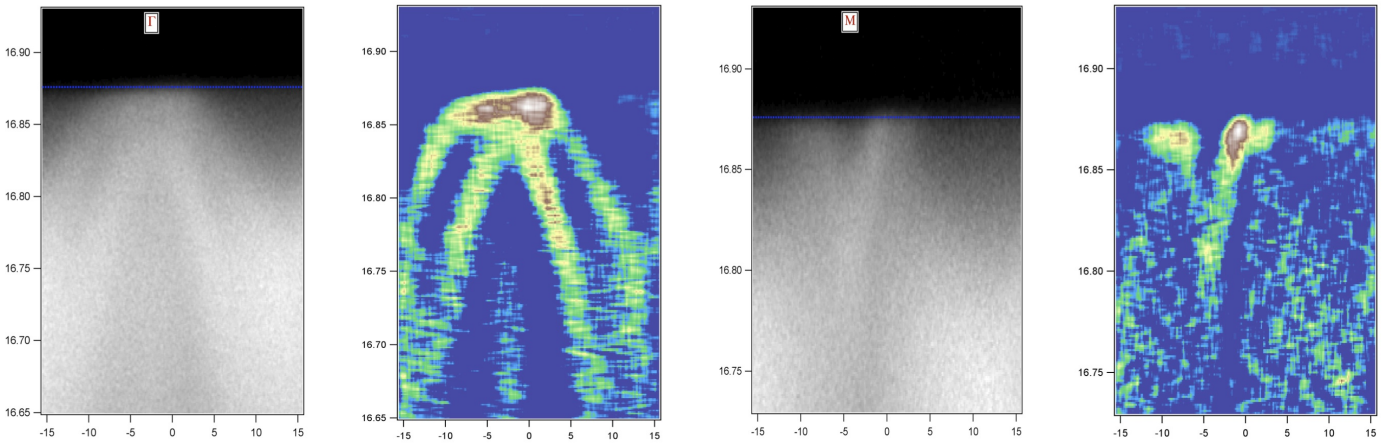

Figure 3.4: *High resolution measurements at the Γ (left) and M (right) points, taken at 15.5K, with a resolution $\Delta E = 13.2\, meV$.*

while the inner band does not and thus could not be observed on the Fermi surface mapping. These two bands have been observed in other Fe pnictides compounds (e.g. $Ba_{0.6}K_{0.4}Fe_2As_2$) and are usually refered to as inner α and outer β bands. As expected for an electron-doped compound, the band structure is "shifted down" with regard to E_F . This results in a smaller hole Fermi surface and a larger electron Fermi surface, with respect to the undoped compound.

Finally, Figure 3.5 shows that the results turn out to be similar to another electron-doped compound of the 122 family measured previously in our laboratory: $BaFe_{1.88}Co_{0.12}As_2$. This similarity is not surprising since basic inquiries on the new Pt doped compound [62] have shown superconducting properties quite similar with other related compounds of the 122 ($BaFe_2As_2$ and $SrFe_2As_2$) family doped with Group VIII elements (including Co, Rh, Ir, Ni, Pd, and

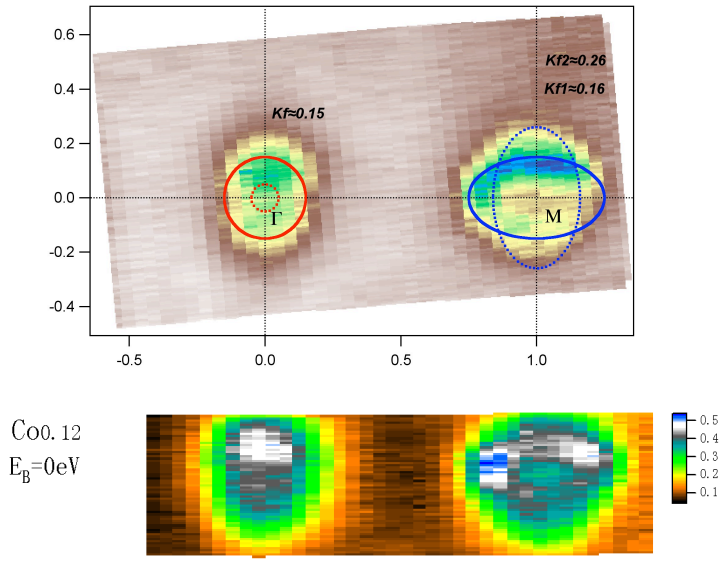

Figure 3.5: *Comparing the Fermi surface results of Pt doped 122 (top) with a previous results for Co doped 122 (bottom). A clear similarity can be observed between the two electron doped compounds, while in the Co case, the FS pockets seem slightly larger.*

now Pt). This study supports the importance of inquiring these various new compounds, by arguing within the scope of the interpocket scattering of electrons via exchange of AFM spin fluctuations that "subtle details and differences among these different series may hold important information regarding the specific mechanism(s) by which magnetic order is suppressed and superconductivity is optimized". The observation of intrinsic variations of T_c themselves in different doping series could carry information of the pairing nature in this family of materials, but our detailed ARPES observations of the FS can certainly bring even more indications in that matter.

3.1.2 Superconducting gap geometry of $NaFeAs_{0.8}P_{0.2}$

This sample is a new compound of the 111 family, with the parent compound NaFeAs and P as the hole dopant. The superconducting transition temperature for this compound is $T_c \approx 33$K. A comment is to be made concerning the conditions of sample preparation. Indeed, the presence of Na in this compound makes the sample very sensitive to outer conditions, for instance the sample has to be conserved under vacuum and sample preparation has to be made in a glove-box with a Na-gas flow to reduce presence of oxygen and water.

First sample (EX7)

Figure 3.6 shows the result for mapping along with the extraction of k_F circle. The mapping does not seem as clear as the previous sample, but we can note the fact that we have a larger electron

Fermi surface with regard to the hole one, as expected for an electron-doped sample. The blue stripped lines linking the inner Γ FS and the hole FS illustrate the nesting phenomenon. It has been found that the maximum electron or hole doping corresponds to a comparable size of respectively the inner and outer Γ FS with that of the hole FS, as can be observed here.

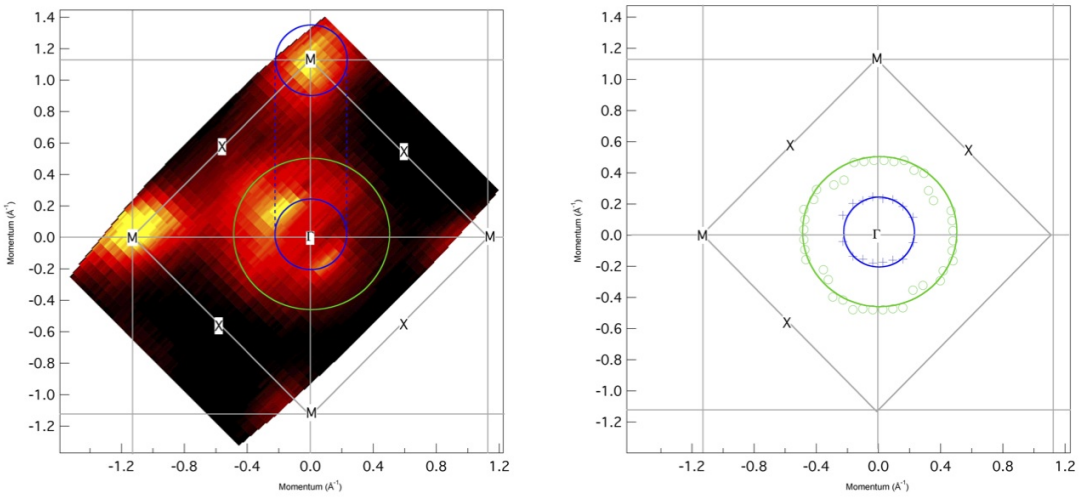

Figure 3.6: *Fermi surface mapping of Na 111 (left) and extraction of k_F from the MDCs (right), measured at 40K.*

Figure 3.7 shows the band dispersion at the Γ point. This time we clearly observe two hole bands crossing E_F . We add a new feature here: the *curvature*, defined as:

$$\frac{\partial^2}{\partial x^2} I \cdot \left(1 - \frac{\partial^2}{\partial x^2} I\right)^{-3/2} \tag{3.1}$$

where x stands for E or k. This is a new tool developed by our group to analyze the band structure. It can be proved on mathematical grounds to be more correct than the simple 2nd derivative.

Temperature dependent measurements were also taken at the Γ point (typically one measurement above and one well below T_c), but these did not show notable and interesting difference, so they are not shown here. In the best condition, one should be able to observe the superconducting gap with a sharp coherent peak in the energy dispersion curves (EDC) at the Γ or M points. The energy resolution at the time of this experiment might not have been good enough for showing this feature.

These results, although consistent with our expectations for 111 samples, do not display any surprising feature. Moreover their resolution appears not to be very high. Indeed, from rough observation of the obtained Fermi surface, its boundaries are far from well defined, with

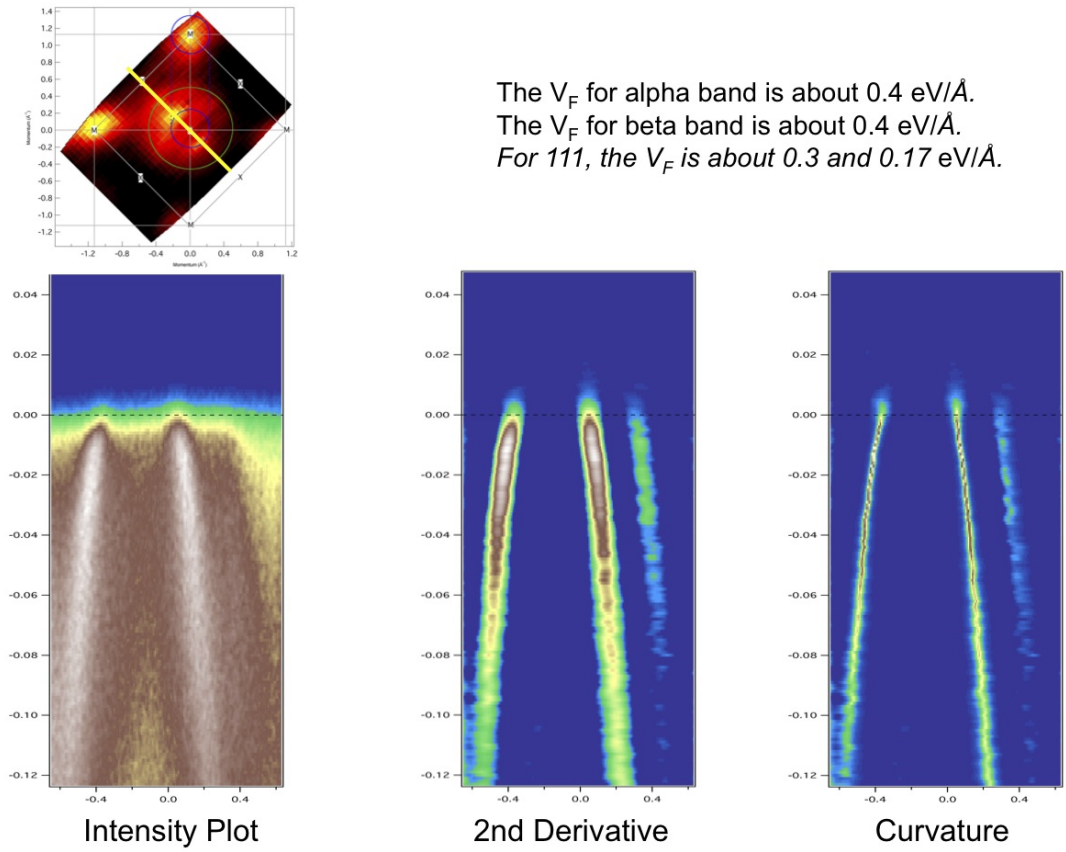

Figure 3.7: *High resolution showing the band dispersion at the* Γ *point. The corresponding cut is shown with the yellow line on the Fermi surface map. The 2nd derivative and the curvature are shown.*

intensity mixing up even between the outer hole and the electron sheets. Looking at the hole sheet, the extracted k_F circles are a bit excentered from the drawn surface sheets. Moreover, its unusually large size suggests a spreading of the surface probably not inherent to the material. The electron sheet geometry is also hard to define. While the measured energy resolution and the expected momentum resolution should be sufficiently good to observe a clearer Fermi surface, we need to look at other factors to explain the results observed. One reason might have been the surface which appeared slightly inhomogeneous after cleaving. Another critical factor is the sample quality, namely having a pure enough single-crystal with a minimum of defects. Lastly, as mentioned before, this compound containing Na is very delicate and may degrade if exposed to ambient air conditions. Although good care was taken during the sample preparation, some details of the method might not be suitable for this sensitive compound, such as the use of liquid graphite to ensure electrical contact between the sample and the holder.

Second sample (Tohoku university)

Following the relatively unsuccessful measurements from our facilities, the sample was measured again at our collaborating laboratory in Tohoku University by Tian Qian, with an energy resolution $\Delta E \approx 5\,\text{meV}$. Here we will only indicatively summarize the results and conclusions, without presenting the data, as the experiment and data analysis were all made by Tian Qian.
For this second sample, our interest was to measure the Fermi surface and the gap geometry near the M point with high precision. In this type of hole-doped sample, observation have been made pointing towards an $s_{\pm}$ gap symmetry (see section 1.2.1). The results indeed turned out of higher quality, with a very clear superconducting gap signature. The gap visible at the M point appeared to be isotropic in the high resolution measurements performed all around the regions where possible nodes are expected. This can be explained by the scenario according to which the node in the gap function occurs half way between Γ and M along k_z, where there is no Fermi surface.

3.2 $Ba_{0.6}K_{0.4}Fe_2As_2$: Bands and Fermi surface orbital character

This section presents the results of polarization-dependent ARPES measurements on the optimally doped superconducting compound $Ba_{0.6}K_{0.4}Fe_2As_2$ (K122). These results were obtained at the SLS synchrotron facility on a beamline scheduled from July 29th to August 6th.

Previous measurements and experiments on iron pnictides' Fermi surface have shown that apart from the global geometry of the Fermi surface — globally accepted as being Fe-3d bands crossing the Fermi level in two to three circular-shaped hole pockets at the Γ point (depending of the k_z value), and two ellipse-shaped electron pockets at M point — non-trivial effects induce variation of the intensity along the different parts of the Fermi surface, even possibly resulting in the impossibility to observe certain pockets. Although this effect is already visible with non-polarized light as in using the gas-discharge lamp sources, it is most clear when using light with different polarizations. This effect is known from the cuprates to be related to the matrix elements $\langle \psi_f^N | \Delta | \psi_i^N \rangle$, as first appearing in equation 2.3. Another form after simplification that we can study more directly is the one-electron dipole matrix elements:

$$M_{f,i}^{k} \propto \langle \phi_f | \mathbf{A} \cdot \mathbf{p} | \phi_{i,k} \rangle \tag{3.2}$$

Indeed, while postponing a detailed analysis of the matrix elements, one can try first considering only the selection rules that bring symmetry constraints on them. These are directly related to the orbital character of the electron involved in the process, and the polarization of the excitation light, thus allowing direct experimental probing.

3.2.1 Direct observation of polarization-dependent selection rules effects

Let us assume a specific geometry for our experiment (see Figure 3.8a), letting the incident light direction and the slit direction forming a plane perpendicular to the sample surface (xy plane), and moreover choosing this plane to lie along a high symmetry line of the crystal (forming a *mirror plane*).

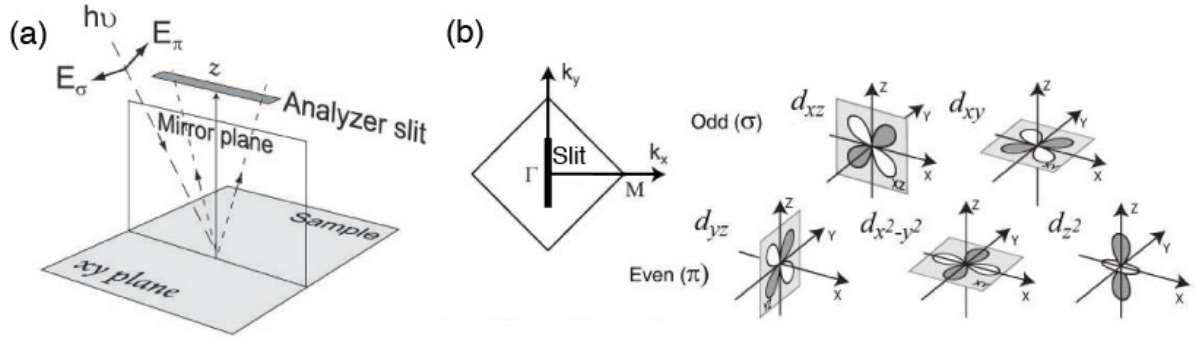

Figure 3.8: **(a)** *Geometry for the polarization dependent experiment* **(b)** *a specific orientation of the sample with the Slit along k_y, and the corresponding symmetries of the five Fe3d orbitals.*

These settings can serve as a ground for simple and direct testing of the near-Fermi level bands' orbital nature using the fact that only overall even symmetry matrix elements give an allowed transition (conversely a transition with odd matrix elements symmetry is forbidden). Knowing that $|\phi_f\rangle$ has even symmetry with regard to the mirror plane without what it would vanish at the analyzer slit, one can only get even-even or odd-odd symmetry for the remaining $\mathbf{A}\cdot\mathbf{p}|\phi_{i,k}\rangle$. While controlling the symmetry of the light polarization, thus of the vector potential $\mathbf{A}$, a certain symmetry for the initial state wave function $\phi_{i,k}$ can be chosen. This is summarized in the following formula:

$$\langle\phi_f|\mathbf{A}\cdot\mathbf{p}|\phi_{i,k}\rangle \quad \text{if } \mathbf{A} \begin{cases} \text{even } (E_\pi)\ \langle +|+|\dots\rangle & \Rightarrow \quad \phi_{i,k} \text{ even} \\ \text{odd } (E_\sigma)\ \langle +|-|\dots\rangle & \Rightarrow \quad \phi_{i,k} \text{ odd} \end{cases} \tag{3.3}$$

where $|+\rangle$ and $|-\rangle$ denote an even/odd state respectively. For a specific orientation with the mirror plane coinciding with the yz-plane (see figure 3.8b), an odd-symmetry (E_σ) light will thus only allow transition from odd-symmetry orbitals d_{xz}, d_{xy}, whereas an even-symmetry (E_π) light will select the even orbitals d_{yz}, $d_{x^2-y^2}$ and d_{z^2}. Here, only the five Fe-3d orbitals are taken into consideration.

The SIS X09LA beamline (see section 2.2.3) has the advantage to provide two directions of linear polarizations: linear horizontal (LH) and linear vertical (LV), respectively named E_π and E_σ in Figure 3.8. These configurations allow us to use advantage of the selection rules described above. However, the energy range for the LV polarization light is limited to $E > 100\,\text{eV}$, energies at which the resolution $\Delta E \approx 25\,\text{meV}$ is not as good as when using $E = 32, 60\,\text{eV} \Rightarrow \Delta E \approx$

8, 15 meV for which most measurements were made when not needing the LV polarization. It should be noted that this orbital test is only valid along a single high symmetry line. However, a given band can have different orbital character along different directions in k-space. This question will be inquired in the next section on Fermi surface polarization dependence, where we will also mention the predictions for such multi-orbital character of the bands along the Fermi surface.

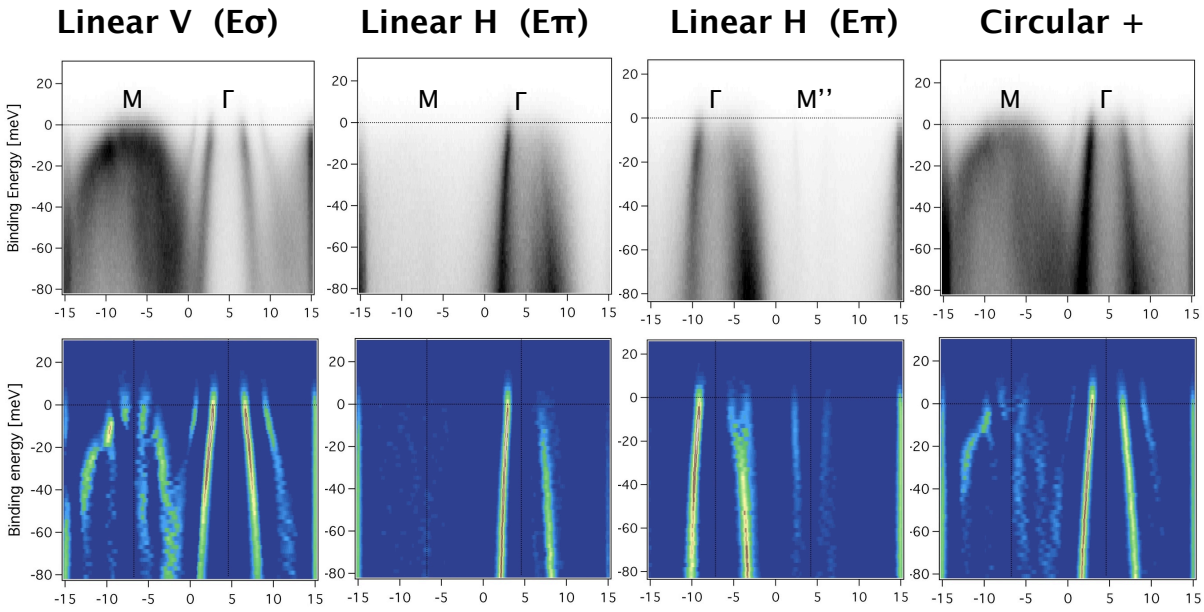

Figure 3.9: *Low energy band structure along the* $\Gamma - M$ *direction, for photon energy* 117 *eV* ($k_z = 0$) *and three different light polarization. The upper graphs show the measured photoemission intensity. The lower graphs display the curvature function as in equation 3.1. The LH case displayed twice corresponds to measurements along the two sides of the* Γ *point.*

For this compound, the lowest available photon energy corresponding to $k_z = 0$ above 100eV is 117 eV. This energy was determined in previous experiments on k_z-dependence (see also the discussion on k_z-dependence in next section). Figure 3.9 gives the high resolution polarization-dependence results in the $M - \Gamma$ direction ($(0, -\pi) - (0, 0)$), with the slit along k_y as in the geometry we determined. The difference between LV and LH polarization EDCs is extremely obvious. In the LV polarization case (E_σ, odd band selection), the M point on the left displays a complex band arrangement below E_F with quite high intensity. The bands appear more clearly on the horizontal curvature graph below, with apparently two electron-like bands, denoted γ (outer) and δ (inner), although the γ band does not appear so obviously. There seems furthermore to be an additional hole-like band at the M point, which might be hybridizing with the γ band. At the Γ point, two bands are clearly visible, denoted β (outer) and α (inner). In the LH polarization case (E_π, even band selection), the γ and δ bands disappear at the M point as well as the β band at the Γ point. An important asymmetry also appears for the α band, which was

not present in the LV case and cannot be explained by our simple selection rules considerations. The two different circular polarization results did not show any remarkable difference, therefore only the C+ polarization is shown. The circular case seems to present a result in-between (or adding up) the LV and LH results in terms of the different bands intensity. This appears reasonable as the polarization vector of the circular light is a combination of the E_π and E_σ vectors, continuously oscillating between them with respect to time and position.
The LV and LH results can be interpreted with regard to the selection rules test described before. First considering the Γ point, the outer β band orbital can be concluded to have odd symmetry, therefore the orbital should be d_{xz} or d_{xy}. The α band appears in both cases, therefore we may expect a mixture of different parity orbitals. At the M point, the single consideration of these results would lead to a conclusion of odd character for both the γ and δ bands. However as this contradicted some of our expectations, a further test was applied by checking the $\Gamma - M$ along the other side of the Γ point ($(0,0) - (0,\pi)$). The result is shown on the third graph of Figure 3.9, and it differs considerably from the previous result: a clear signature of the γ band is visible, while the δ band is still invisible, which seems to mean that the character of the γ band might be of mixed odd and even symmetry. However, with the band possibly undergoing a hybridization in Figure 3.9, the symmetry is not so obvious.

We subsequently checked the same line for $k_z = \pi$, which corresponds to photon energy 138 eV. The results are shown in Figure 3.10. As the signal strength becomes weaker when increasing energy in this range, the parameters were set more "rough" to partly compensate for the decrease of photoemission intensity, resulting in a worsening of the resolution ($\Delta E \approx$ 30 meV). The results for the band symmetries appear rather similar to the 117 eV case, with a few small differences. The most notable difference is the apparent inversion of the intensity assymetry in the LH and C$\pm$ cases, it is now the right hand side band which appears with higher intensity. Besides, the signature of the γ band is visible for LH polarization, while in the LV case the band seems slightly weaker.
A surprising effect is that the measured $k-$range seems to have gotten smaller than in the 117 eV case, contrarily to the basic expectation of photo energy increase. This is visible in the fact that the center of the Z and A points got further away from each other. However, the bands on the right side of the Z point seem closer to each other, while on the left side the distance seems comparable to previously. The k_z dispersion can be playing a role in this, although only a minor variation of the Fermi surface size is for instance expected, probably not totally accounting for the apparent "spreading" of the band structure over a larger k-range.

Another line of interest is the high symmetry $X - \Gamma$ line ($(-\pi/2, -\pi/2) - (0,0)$). For this new direction, the orbital symmetry as defined in Figure 3.8 need to be revised. The $d_{x^2-y^2}$ orbital is odd with regard to the new symmetry plane (see Figure 3.11), while the d_{xy} and d_{z^2} are even. The symmetry of the two remaining orbitals d_{xz} and d_{yz} is however neither odd nor even. It can be seen however that a combination of these orbitals answers the desired symmetry,

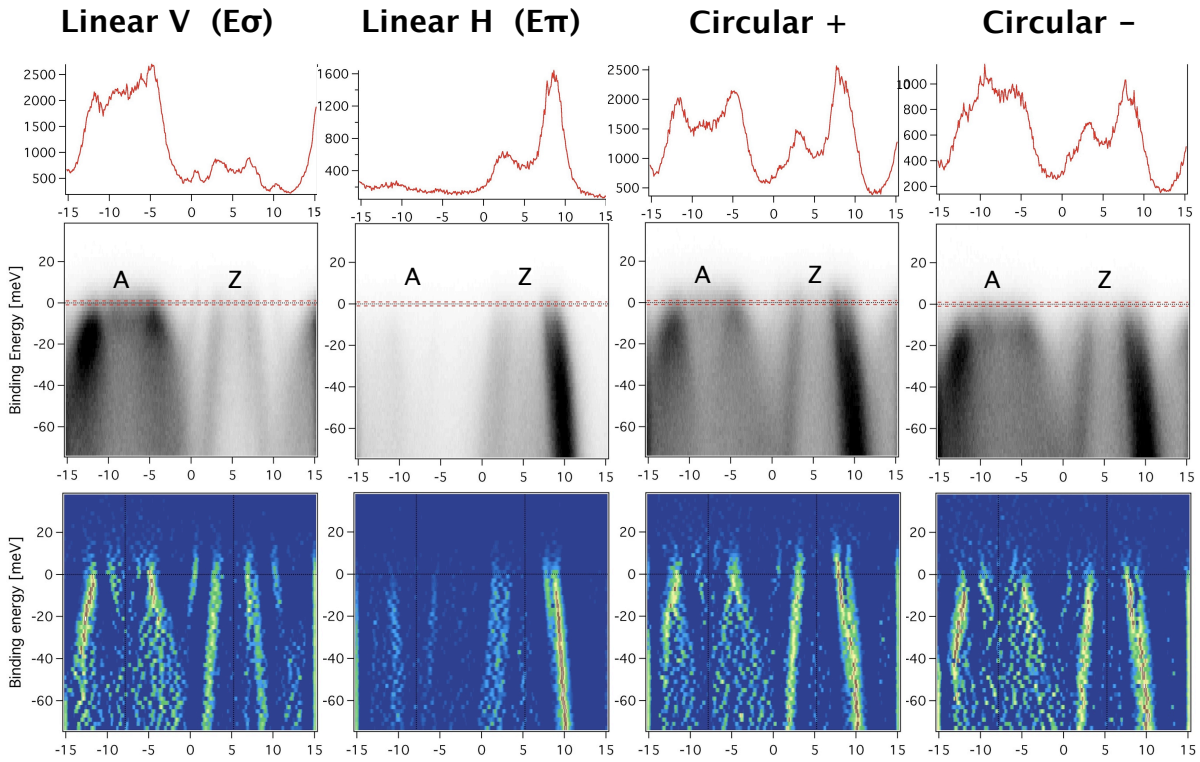

Figure 3.10: *Low energy band structure along the $M-\Gamma$ $(A-Z)$ direction for the photon energy 138 eV. On the first row of subgraphs, the MDCs near the Fermi level are displayed. The y-axis corresponds to the summed number of counts and can be used to compare the intensity of the different bands in for different polarizations. The middle row is the photoemission intensity and the lower row the curvature function.*

and can be candidate to identification by the bands.

The results are summarized in Figure 3.12, with again the photoemission intensity graphs ac-

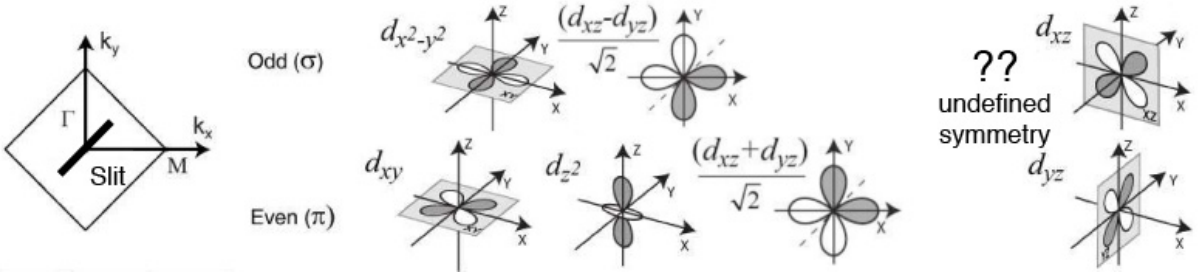

Figure 3.11: *Definition of the orbitals symmetry in the $X-\Gamma$ geometry.*

companied by the curvature plots. All graph display the first Brillouin Zone Γ point on the right hand side, while on the left, the Γ of the second Brillouin zone (named Γ') is visible. At photon energy 117 eV ($k_z = 0$), only the LH and LV polarization measurements were taken. In the LH polarization case (a), two hole-like bands are visible on each side of the Γ point,

although apart the inner left branch of the α band, all other three have very weak intensity and are only made visible by the curvature. The corresponding Γ' point on the left seems to display slightly different informations. The right branch of both α and β bands are clearer (less diffused), thus giving a higher intensity on the curvature graph. Judging from the opening at the Fermi level, the left branch might be the outer β band which would mean the α band is not visible, in contrast to the Γ point. If it is the α band, it would mean the size of Γ' (the band separation at E_F) is slightly larger than Γ. This could result from a slight misalignement out of the $\Gamma - X$ direction. In the LV polarization case at the Γ point, the inner α band is well defined with high intensity and an asymmetry towards the left/right branch of the Γ/Γ' point. The β band is again visible at the Γ point with weak intensity. The band on the left side of Γ' seems to cross E_F at a similar k than in the LH case, but the band shape seems to denote an inner α band. The strong intensity band on the right side seems to be located in-between the α and β bands of the LH case. It might thus be the α' third hole-like band, but most probably it is either one or the other of the α and β bands. The asymmetry in the LV case is surprising here. Indeed, it comes as an exception among all LV results presented before and these to come. It seems thus intuitively reasonable to have no asymmetry for the LV light, as the polarization direction is perpendicular to the incoming direction, inside the xy-plane and normal to the slit direction.
These results seem to suggest a mixed symmetry nature for the α band, which appears with relatively high intensity in both case, while the conclusion for the β band is less obvious. Only one hint in favour of an even symmetry is present with the clearer definition on the right side and perhaps the left side of Γ' in the LH polarization case.
A comment should be made about the Γ' point. It has been assumed here that the Γ' point (at the (π, π) position) is of "Γ" nature, that is, with $k_z = 0$. However this is not fully correct, as will be seen in a further analysis in next section (in particular, see equation 3.7). Actually, at $\mathbf{k}_{\parallel} = (\pi, \pi)$, k_z can be shown to be located in-between 0 and π. This may explain the difference size of the Γ' point, and the difference in the bands intensity.

The results for photon energy 138 eV ($k_z = \pi$), displayed on the right hand side of Figure 3.12 again suffer a lower intensity, but the bands are still distinguishable. The LH polarization case presents an interesting phenomenon at the left side of the Z point, with a mixture of perhaps up to three bands visible. On the right side of the Z point, if one trusts the curvature function which clears out the broad intensity pattern, a single band could be identified as the middle α' or the β band. However, the broad intensity suggests a mixture of at least two bands. Around the Z' point, apparently the α and β band are distinguishable. An interesting thing can be seen: the LV polarization single band at Z aligns perfectly with the inner-most of the "three bands" visible above on the LH graph. It thus corresponds quite convincingly to the inner α band. On the other hand the LV right branch clearly does not align well with the LH band above, thus

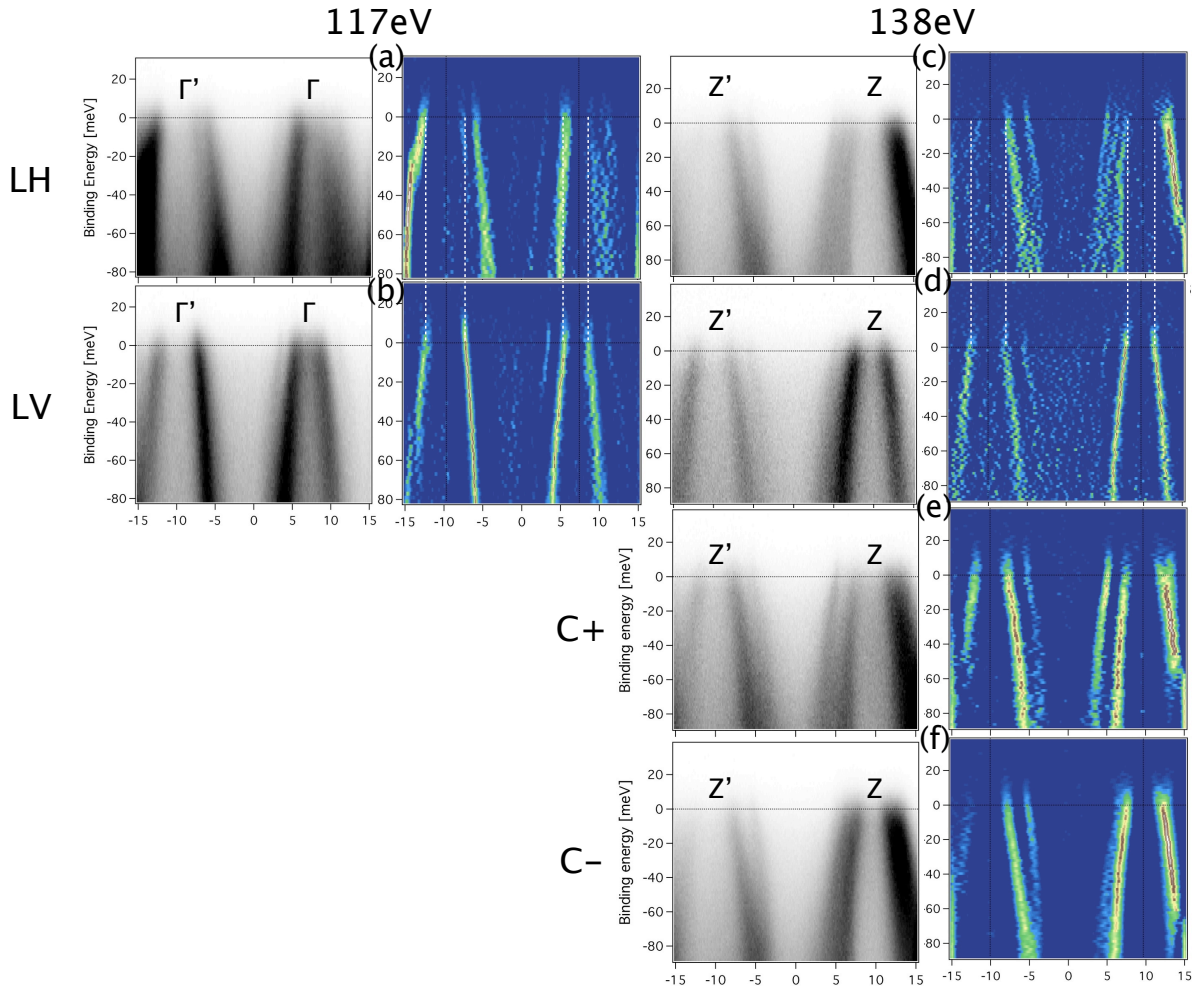

Figure 3.12: *Low energy band structure along the $X - \Gamma$ direction, for photon energy 117 eV and 138 eV. The polarization is displayed by rows: the first row is the results for LH, the second row for LV, etc. The vertical dashed lines are given to help comparing the band positions in the LH and LV cases.*

pointing towards an α' or β nature of the LH band. No obvious asymmetry between the left and right branches is visible in the LV case, making the inner α band at the Z' point clearer, at the same position at the trace visible in the LH case above.

From these considerations, the conclusion seems clear for the inner-most α band to be of odd symmetry, thus $d_{x^2-y^2}$ or the combination $d_{xz} - d_{yz}$ described before. Similarly, the middle/outer bands with clearly high intensity in the LH case are not visible in the LV case, thus concluding for an even symmetry: d_{xy}, d_{z^2} or $d_{xz} + d_{yz}$.

Although the conclusions made using 138 eV photons seem more clear, they are compatible with these of the 117 eV case. Besides, different conclusions are possible as a certain difference is expected between $k_z = 0$ and $k_z = \pi$. For instance, three bands have been measured before at $k_z = \pi$, an interpretation to which can be that the α band visible otherwise might be the

hybridization of two bands. As the inner and middle bands α, α' are expected to have opposite symmetries as will be seen in the next section, a hybridization would explain the fact that the α band is visible in both LH and LV polarizations.
The conclusions about the bands at the Γ/Z point in the $X-\Gamma$ direction can be considered jointly with these of the $M-\Gamma$ direction. This is done and summarized in Table 3.1.

Pos	Band	$M-\Gamma$	$X-\Gamma$	Joint conclusion
Γ	α (117eV)	mixed parity	mixed parity	?
	α (138eV)	mixed parity	$\|-\rangle$: $d_{x^2-y^2}$ or $d_{xz}-d_{yz}$	$d_{x^2-y^2}$ or d_{xz}/d_{yz}
	α' (138eV)	$\approx$mixed parity	$\|+\rangle$: d_{xy}, d_{z^2} or $d_{xz}+d_{yz}$	d_{xy}, d_{z^2} or d_{xz}/d_{yz}
	β (117eV)	$\|-\rangle$: d_{xz} or d_{xy}	$\approx\|+\rangle$: d_{xy}, d_{z^2} or $d_{xz}+d_{yz}$	d_{xy} or $\approx d_{xz}/d_{yz}$
	β (138eV)	$\|-\rangle$: d_{xz} or d_{xy}	$\|+\rangle$: d_{xy}, d_{z^2} or $d_{xz}+d_{yz}$	d_{xy} or $\approx d_{xz}/d_{yz}$
M	γ	$\approx$mixed parity	–	?
	δ	$\|-\rangle$: d_{xz} or d_{xy}	–	d_{xz} or d_{xy}

Table 3.1: *Symmetry conclusions summary. The "$\approx$" signs indicate uncertain conclusions.*

3.2.2 Influence of polarization on Fermi surface topology

In the preceding section, observations and conclusions where made on the orbital nature of a given band occuring in EDCs along high symmetry lines, based on direct selection rules considerations and for linear polarization light only. However, instead of observing a single EDC along a high symmetry line, one can take advantage of the powerful Fermi surface mapping abilities of the high intensity and high momentum resolution synchrotron light, to observe polarization-dependence of the whole Fermi surface. This part will present the results of Fermi surface mapping in the $M-\Gamma$ direction, for photon energy 117 eV ($k_z = 0$) and for two different polarizations LH and LV. These results will be compared to Fermi surface orbital character simulations as described below. From the comparison of the experimental results with the simulations, conclusions will be drawn regarding the Fermi surface orbital character, and the subject of Fermi surface k_z-dependence will be approached.

In terms of selection rules, one has to elaborate the test used before in order to make predictions or analyze the change of Fermi surface with polarization. In this regard, simulations for orbital character are being made in our group [63], the comparison with which was also one of the main motivations to perform these orbital character measurements. These will mostly be mentioned as a theoretical comparison for our measurements, where some correspondences were found as well as a number of inconsistancies, the work being still in progress. Without entering the details of this other project, the main ideas and assumptions of these simulations can be summarized as follows:

Definition of a new experiment geometry To treat the polarization-dependent measurement of a whole Fermi surface, the symmetry has to be defined according to a different

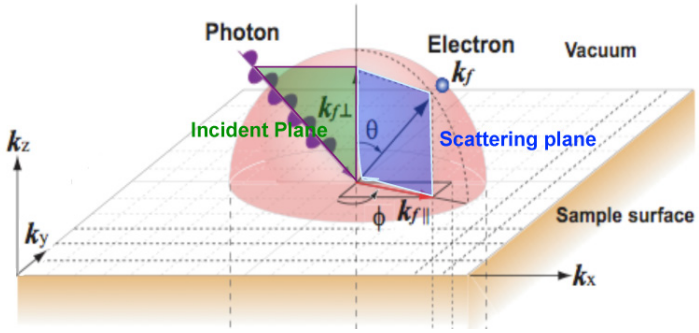

Figure 3.13: *General definition of the geometry for selection rules along any direction.*

point of view. Indeed, as soon as one gets off the central high symmetry line, the sample rotation results in the non validity of the mirror plane definition. A convenient geometry is that of Figure 3.13, with the definition of the *incident plane/scattering plane*, spanned respectively by the photon/photoelectron momentum and the surface normal. Understanding that both k_i and k_f must lie in the scattering plane, it is natural that the orbital symmetry and thus the light polarization symmetry be defined with respect to that plane.

Modelling the wave function symmetry A critical and delicate step is to model the wave function symmetry. Indeed, now considering two continuous dimensions, a "discrete" definition of symmetry parity even or odd is not convenient, we shall thus consider a wave function as a linear combination of even and odd states:

$$|\psi_i\rangle = a|+\rangle + b|-\rangle \tag{3.4}$$

A general expectation for the photoemission intensity dependence on the selection rules can be derived, where the selection rules can once again be applied by determining the symmetry of the five 4 symmetry axes: $\Gamma - M$ $(0,\pi)$, $\Gamma - M'$ $(\pi,0)$, $\Gamma - X$ (π,π), and $\Gamma - X'$ $(\pi,-\pi)$ and projecting $\mathbf{A}\cdot\mathbf{p}$ along 3 directions: x_p in the xy plane and parallel to the scattering plane, x_s in the xy plane and perpendicular to the scattering plane, x_z perpendicular to the xy plane. The resulting formula for the photoemission intensity selection rule components can be written as:

$$I \propto |\langle\psi_f|\mathbf{A}\cdot\mathbf{p}|\psi_i\rangle|^2 = |A_p a + A_s b + A_z a|^2 \tag{3.5}$$

Fermi surface experimental geometry and main orbital contributions assumptions The K122 compound has been subject to much research already, settling a good idea about its Fermi surface geometry with two (three) concentric circular hole-like pockets at the Γ (Z) point, and two ellipticoidal electron-like pockets at the M/R point.

Following the previous proposition in equation 3.4 for the symmetry expression of any

wave function, we can thus model the five Fe3d orbitals along these circular Fermi surfaces as:

$$
\begin{aligned}
d_{xy} &= \cos 2\varphi|-\rangle + \sin 2\varphi|+\rangle & \mathrm{d}_e &= \cos\theta d_{xz} + \sin\theta d_{yz} \\
d_{yz} &= \cos\varphi|-\rangle + \sin\varphi|+\rangle & \mathrm{d}_o &= -\cos\theta d_{yz} + \sin\theta d_{xz} \\
d_{xz} &= \cos\varphi|+\rangle - \sin\varphi|-\rangle & \mathrm{d}_{mf1} &= \tfrac{\cos 2\theta'+1}{2} d_{xy} + \tfrac{-\cos 2\theta'+1}{2} d_{yz} \\
d_{x^2-y^2} &= \cos 2\varphi|+\rangle \sin 2\varphi|-\rangle & \mathrm{d}_{mf2} &= \tfrac{\cos 2\theta'+1}{2} d_{xz} + \tfrac{-\cos 2\theta'+1}{2} d_{xy} \\
d_{z^2} &= |+\rangle
\end{aligned}
\tag{3.6}
$$

where φ is the angle between the scattering plane and the xz-plane, thus describing the symmetry in a 360° emission orientation along the whole Fermi surface. The model functions with the parameters θ, θ' on the right hand side are the predicted orbital components as shown in Figure 3.14b/c, based on the d_{xz}/d_{yz} orbital combinations already introduced in the previous section (see Figure 3.11).

Lastly, some assumptions need to be made regarding the orbital character of the different Fermi surface parts in order to perform the simulation for the intensity patterns. From LDA calculations [20] and previous experimental results, predictions are made on the Fermi surface orbital composition as in Figure 3.14a, with our own modified expected orbital scheme in Figure 3.14b/c.

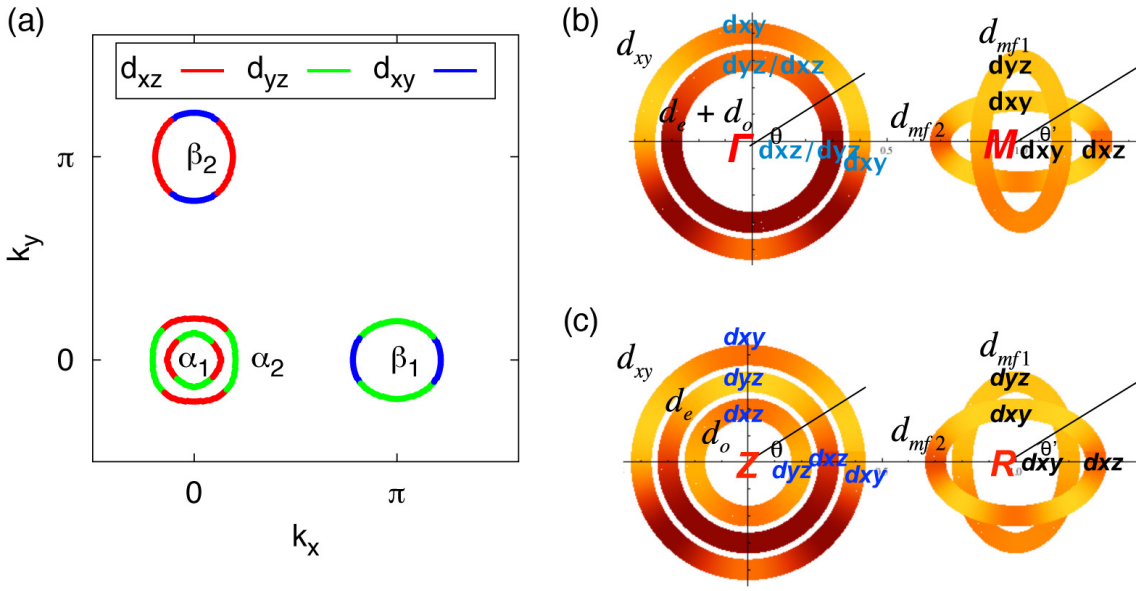

Figure 3.14: *Orbital predictions for the Fermi surface.* **(a)** *Orbitals as from LDA calculations. The two M points are displayed unfolded. Figure reprinted from reference [21] (results originally obtained by Graser* et al. *[20]).* **(b)** *Modified folded orbital predictions for the* Γ *and M points.* **(c)** *Same for the Z and R points.*

It is to be understood that although the symmetry-modelling formula we have defined (equation 3.6) can in principle be used to describe symmetry in all directions, the light direction should still

be chosen along a high symmetry line. Indeed the light direction is determined experimentally for each sample by making a fast "alignement" mapping. It is thus easier to settle the light direction in a direction between two Fermi surface sheets' centers. The direction so settled can then be used to perform simulations, which can be compared with the mapping results.

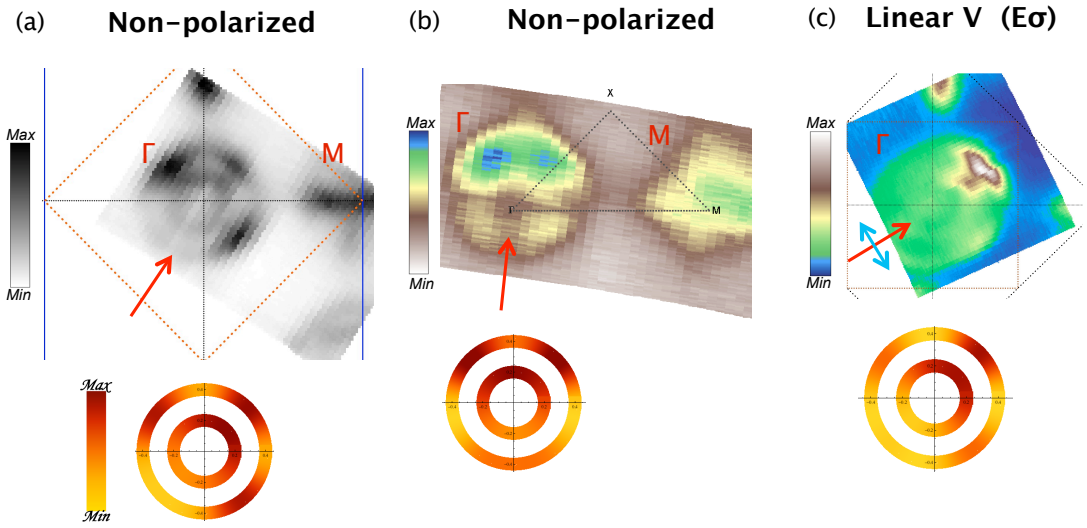

Figure 3.15: *Comparison of FS simulations and experimental results at the* Γ *point.* **(a)** *and* **(b)** *were obtained in* $\Gamma - X$ *and* $\Gamma - M$ *directions respectively at our laboratory using a Helium lamp with photon energy 21.2 eV.* **(c)** *was obtained in* $\Gamma - X$ *direction at SIS synchrotron with photon energy 30 eV. The incoming light and polarization direction are indicated with red and blue arrows respectively. The color gradients indicates different photoemission intensities as described by the scale bars on the left side of the graphs.*

Figure 3.15 shows experimental results previously obtained at our laboratory and at the SIS beamline. The corresponding simulations using the method described above are shown on the lower part of the graphs. The correspondence at the Γ point is remarkable in all three cases, with a quite correct prediction of the intensity patterns. For the ***(a)*** and (b) results, as the sample cannot be rotated in the xy-plane with our manipulator, the orientation deviates slightly from the desired axis.

Figure 3.16 shows the results for mapping with incoming light in the $M - \Gamma$ direction. The photon energy is 117 eV ($k_z = 0$). This results comes as a generalization of the band structure measurements done in the previous section along the same high symmetry line. The top parts of the figure correspond to the experimental Fermi surface mapping. The Fermi surface polarization dependence appears very clearly between the left and right graphs. The disappearance of the bands at the M point observed before (see Figure 3.9) is confirmed here at the position below the Γ point (sitting at the upper-right side of the FS) where no band visibly crosses the Fermi level. The FS geometry of the Γ point is uncovered. It has a clearly anisotropic inner FS pocket corresponding to the α band and an outer FS pocket corresponding to the β band. The

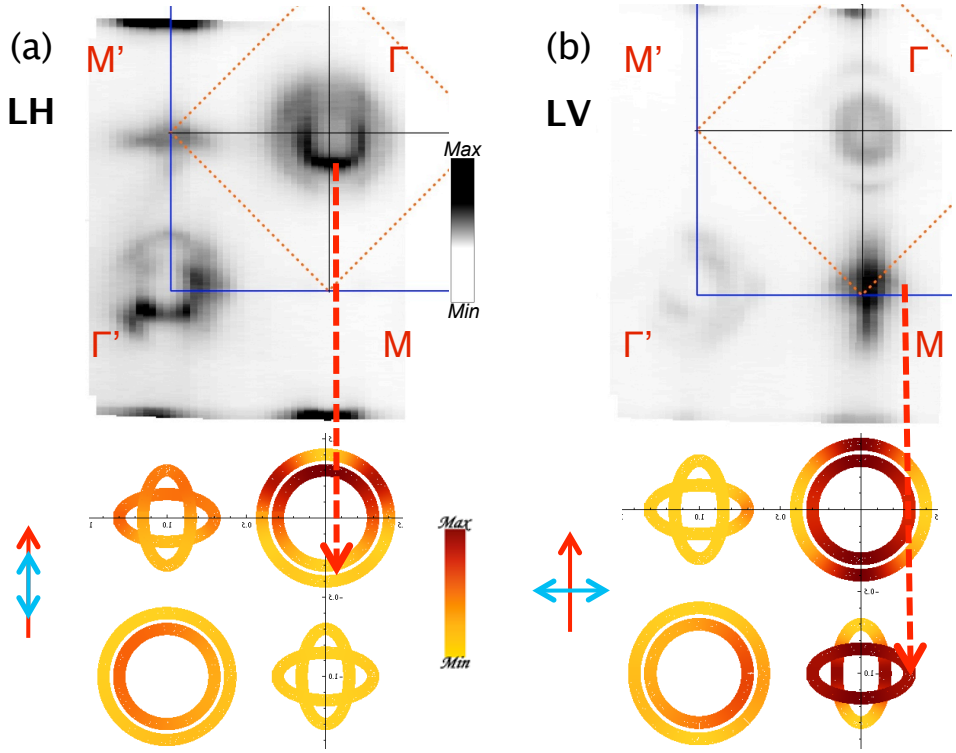

Figure 3.16: *Comparison of mapping with LH* **(a)** *and LV* **(b)** *polarization lights (upper graphs) and their corresponding simulations (lower graphs), for photon energy* 117 *eV. The light incoming (polarization) direction is indicated by the red (blue) arrow on the left side of the simulation graphs. The dashed red arrows denote weaknesses of the simulations.*

latter could not be observed along the single line measurement before. The geometry of the Γ' point on the lower-left part of the graph differs from that of the Γ point, while its intensity is comparable to that of the Γ point. The two bands can also be distinguished, with the intensity a four corners-pattern, suggesting a departure from a purely circular shape for the hole-like FS pockets. The M' point on the left side of the Γ point displays at cross-like pattern, with a preference for the $M' - \Gamma$ direction. In the LV polarization case, the situation for the M, M' points seems "inverted". As known from the high symmetry line measurement before, the bands at M point appear with a high intensity. The band crossing the Fermi level result in a visible FS pocket at the M point, although it is hard to distinguish the two γ and δ bands. This appearance of the FS at the M point coincides with the disappearance of the one at the M' point. The two bands visible at the Γ point have a clear symmetry along the light direction as observed before for LV polarization light.

As it is not possible to make direct use of the selection rules when going off a high symmetry line (where the incident and scattering planes do not correspond to a mirror plane, such as along the $\Gamma' - M'$ line), we shall use the simulations in the lower part of Figure 3.16. The first observation is that the simulations correctly predicts the disappearance of the M point in the LH case.

In the LV case however, at the M point, a discrepancy is visible and denoted by the dashed red arrow. The intensity is predicted to be high all along the horizontal ellipsoidal FS pocket (corresponding to the δ band previously defined, with "inner" position when measured along the $M-\Gamma$ direction) and the middle part of the vertical γ pocket. Indeed, the orbital chosen for these parts all having odd symmetry (see Figure 3.14). However, the measured intensity at the M point seems to favor the vertical pocket γ. This seems to mean that our prediction for the multi-orbital character of the M point is not fully correct. As the FS pocket at the M point is near a high symmetry line, we can tentatively conclude that the outer left and right "wings" of the horizontal pocket δ should be of even symmetry. The orbital character of the bands at the M point will be further inquired below. At the M' point, the simulation reproduces quite well the less intuitive asymmetry of the LH/LV cases, with almost no intensity in the LV case, and a moderate intensity in the LH case. However, the specific geometry of the FS pockets in the LH case again does not fully match the experimental results.
At the Γ point, our simulations differ notably from the experimental results. Indeed, the intensity is predicted higher on the upper side of the FS pocket, but the measured intensity follows an opposite trend, as denoted by the dashed red arrow. Similarly, the prediction for the inner band at the Γ' point seems opposite to the measured intensity, which might be related to the same vertical asymmetry inversion problem. In the LV case, no vertical asymmetry is observed in the measured FS, in good correspondence with the simulation. The predictions at the Γ' point also seem to correspond reasonably well to the experimental results. The asymmetry problem along the vertical direction (more probably related to the incoming light direction) will be seen to be related to the k_z dependence of the Fermi surface, in a next part analyzing photon energy-dependent results.

The simulation results using the orbital prediction for the M point as described in Figure 3.14 seemed to differ from the experimental results. Therefore, we may like to inquire different orbital scenarios. Figure 3.17 shows different scenarios of orbitals combination at the M point and the corresponding simulated FS. From simple comparison between the different simulated FS pattern and the measured FS on the left, the best correspondence would be with the (b) or (d) case. The conclusions from the previous section tell us that at the crossing of the horizontal δ band with the $M-\Gamma$ axis, the orbital character should be odd. However, this is not the case for the d_{yz} orbital proposed by both the (b) and (d) scenarios. This seems to bring a contradiction between our simulation model and the predictions made by theory, as no combination of the predicted orbitals d_{xz}, d_{yz} and d_{xy} as in Figure 3.14a gives a good correspondence with the experiment.

As a second important discepancy, the intensity asymmetry observed in the LH polarization light case was found inverted between our simulations and measurements. Moreover, it has seemed to vary while using different photon energies in a number of data that are not displayed here. This suggests a systematic inquiry of the photon energy dependence in order to determine

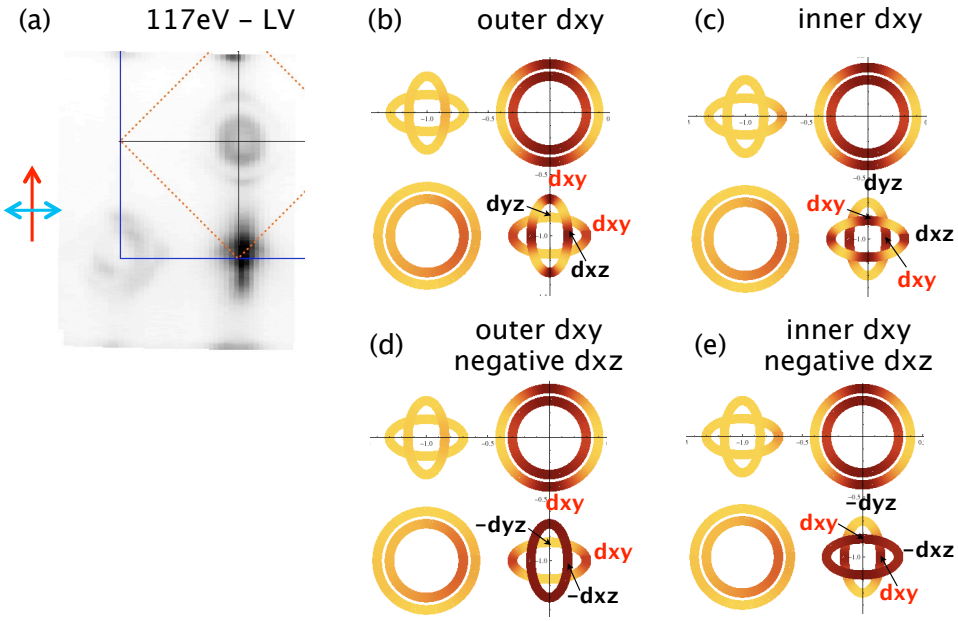

Figure 3.17: *Simulation for different orbital character hypotheses at the M point.*

the trend of these changes.

It is known that the band structure of the pnictides is k_z dependent in contrast with the cuprates, due to the overlap of orbitals along the k_z direction. The k_z dependence exists in several regards. A change in the whole Fermi surface geometry, with the diameter of the pockets at our Γ and M points definition oscillating with k_z, was observed in the $BaFe_2As_2$ parent compound [40], and in the electron doped $BaFe_{2-x}Co_xAs_2$ ($x = 0.18, 0.2$) compound [40, 39]. In the superconducting state, the superconducting gap is also k_z dependent, as has been proposed most recently in a paper from our group by Y.-M. Xu [42]. Moreover, at given regular values of k_z corresponding to the periodicity $k_z = n\pi/c$ although needing some phenomenological adjustments[2], a change in the band structure reveals a third band at the Z point [42] as predicted by theory. All the effects mentioned above are related to a periodical change of the band structure along k_z. The kz component is often approximated as [64]:

$$k_z = \sqrt{\frac{2m}{\hbar^2}} \cdot \sqrt{(\hbar\omega - \Phi - E_B)\cos^2\theta + V_0} \tag{3.7}$$

where apart from the usual parameters for photoemission, V_0 is the inner potential of the sample and θ describes the emission angle of photoelectrons relative to the sample's surface normal. As a consequence of the k_z formula's θ-dependence, different regions of the BZ in a Fermi surface map correspond to different k_z. We will thus focus on the Γ point region where $\theta \approx 0$, and for

[2]As described in section 2.1.3, the $k_\perp$ or k_z component is not conserved in the photoemission process, thus cannot be infered from a simple linear relation to the photon energy.

energies known to correspond to the "$k_z = \pi$", or k_π. The values 117 eV, 138 eV used before were determined experimentally but are well satisfied by equation 3.7 when fitting the parameter values for the K122 sample : $k_z \approx 0.512\sqrt{(\hbar\omega - 4.4) + 15}\,[\text{Å}^{-1}]$, with $\hbar\omega$ in [eV].

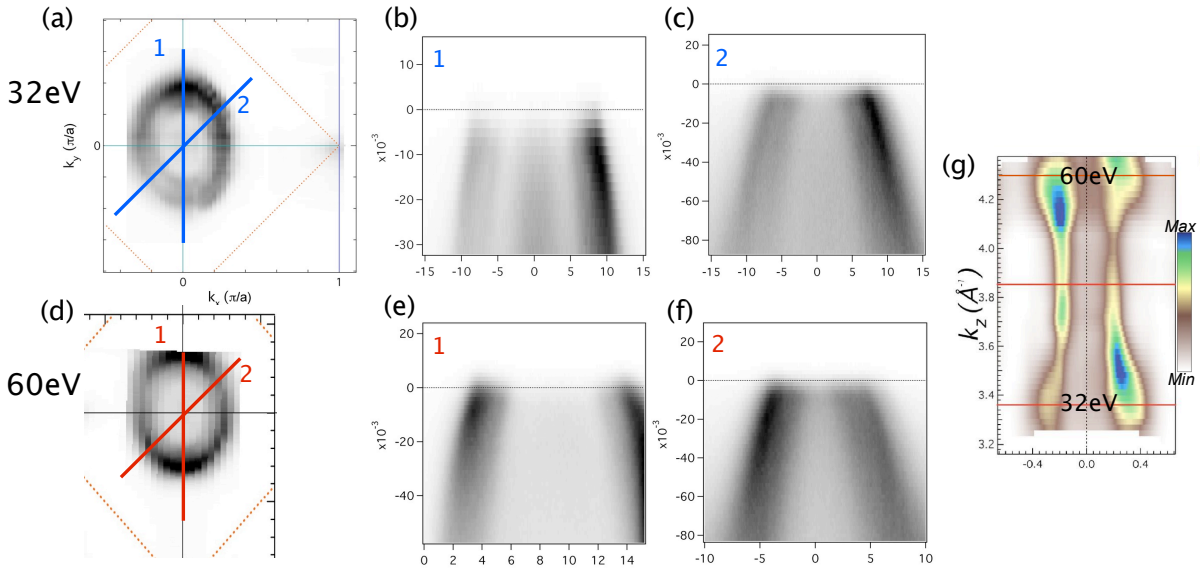

Figure 3.18: *Photon energy dependence of the Fermi surface intensity for LH polarization light.* **(a)**, **(d)** *Fermi surface mapping at photon energy 32 eV and 60 eV, respectively.* **(b)**, **(e)** *band structure in the $M - \Gamma$ direction for photon energy 32 eV and 60 eV respectively.* **(c)**, **(f)** *band structure in the $X - \Gamma$ direction for photon energy 32 eV and 60 eV respectively.* **(g)** *k_z-dependence of intensity at Fermi surface (Figure* **(g)** *reprinted from an ongoing research project by Y.-M. Xu).*

Figure 3.18 presents the Fermi surface results for photon energy 32 and 60 eV respectively giving $k_z = 3.34, 4.3\,\text{Å}^{-1}$, corresponding to the Z point position. The discrepancy between both photon energies is visible in the intensity pattern in parts (a) and (d) of the graph. In the 32 eV case, the intensity is weaker on the left branch than the right branch. At 60 eV, the situation reverses in the $X - \Gamma$ direction, while in the $M - \Gamma$ direction the intensity is about equal on both sides. This effect confirms previous k_z-dependence research by Yi-Ming Xu (see 3.18g). The effect uncovered here is the inversion of the asymmetry regime from 32 to 60 eV photon energy. The contrasts with $2\pi/c$-"periodic- behaviour" in this k_z range of quantities like the Fermi surface size (in parent and electron doped-compounds) and the superconducting gap.

Conclusion

The main research on the bands and Fermi surface orbital character of the compound $Ba_{0.6}K_{0.4}Fe_2As_2$ have brought several conclusions.

In the first results part, direct observation of the selection rules effects was made with high resolution polarization-dependent measurements along the high symmetry lines. This test using simple symmetry considerations already brought some restrictions on the orbital character of the different bands. Furthermore, it made clear that mixed orbitals need to be considered in the description of the bands.

In the second part, the selection rules test was extended to the whole Fermi surface. Some examples of previous experiments at our laboratory were presented that show good agreement with the simulations results. The Fermi surface was obtained from mapping with LH and LV light polarization. From the comparison of the experimental results with orbital character simulations, conclusions have been made regarding the orbital character of the bands at the Γ and M points. This gives restrictions on the possible orbital character of the bands. In addition to that, the band orbital character at the M point was further inquired but seemed to show a contradiction, probably indicating a weakness in the simulation way. The comparison of experimental results and simulations also underlined a complex k_z-dependence effect, which periodicity — if there is — might be double of that of the Fermi surface geometry change as inquired in different works. This effect is probably related to the non-trivial matrix elements photon energy dependence. These results suggest the need to include the matrix elements in our orbital character simulations, in order to include these k_z-dependent effects.

It should be recalled that these results of orbital characterization of the K122 compound have been obtained in a single experiment. It is also the first experience in comparing polarization-dependent results with our simulations. Besides our conclusions, these new results thus naturally raised several questions. Answering these may require further experiments.

Bibliography

[1] *Possible High T_c Superconductivity in the* Ba-La-Cu-O *System*, J. G. Bednorz and K. A. Muller, Z. Physik B 64, 189 (1986).

[2] *BCS theory of superconductivity: it is time to question its validity*, J. E. Hirsch, Phys. Scr. 80, 035702 (2009).

[3] *Nodal structure of unconventional superconductors probed by angle resolved thermal transport measurements*, Y. Matsuda, K. Izawa, and I. Vekhter, J. Phys.: Condens. Matter 18, R705 (2006).

[4] *Iron-Based Layered Superconductor* $La[O_{1-x}F_x]FeAs$ *($x = 0.05 - 0.12$) with $T_c = 26\,K$*, Y. Kamihara,T. Watanabe, M. Hirano, and H. Hosono, J. Am. Chem. Soc. 130, 3296 (2008).

[5] *Iron-based layered superconductor:* LaOFeP, Y. Kamihara, H. Hiramatsu, M. Hirano, R. Kawamura, H. Yanagi, T. Kamiya and H. Hosono, J. Am. Chem. Soc. 128, 10012 (2006).

[6] *Superconductivity in* LnFePO *(Ln=La, Pr and Nd) single crystals*, R. E. Baumbach, J. J. Hamlin, L. Shu, D. A. Zocco, N. M. Crisosto and M. B. Maple, New J. Phys. 11, 025018 (2009).

[7] *Angle-resolved photoemission spectroscopy of the cuprate superconductors*, A. Damascelli, Z.-X. Shen, Z. Hussain, Rev. Mod. Phys. 75, 473 (2003).

[8] *To What Extent Iron-Pnictide New Superconductors Have Been Clarified: A Progress Report*, K. Ishida, Y. Nakai and H. Hosono, J. Phys. Soc. Jpn. 78, 062001 (2009).

[9] *An overview on iron based superconductors*, P. M. Aswathy, J. B. Anooja, P. M. Sarun and U. Syamaprasad, Supercond. Sci. Technol. 23, 073001 (2010).

[10] *Magnetism in Fe-based superconductors*, M. D. Lumsden and A. D. Christianson, J. Phys.: Condens. Matter 22, 203203 (2010).

[11] *Strong Correlations and Magnetic Frustration in the High Tc Iron Pnictides*, Q. M. Si and E. Abrahams, Phys. Rev. Lett 101, 076401 (2008).

[12] *Pairing Symmetry in a Two-Orbital Exchange Coupling Model of Oxypnictides*, K. J. Seo, B. A. Bernevig, and J. P. Hu, Phys. Rev. Lett. 101, 206404 (2008).

[13] LaFeAsO *as a Self Doped Spin-1 Mott Insulator: Quantum String Liquid State and Superconductivity*, G. Baskaran, J. Phys. Soc. Jpn. 77, 113713 (2008).

[14] *Normal-state correlated electronic structure of iron pnictides from first principles* L. Craco, M. S. Laad, S. Leoni, and H. Rosner, Phys. Rev. B 78, 134511 (2008).

[15] *Bandwidth and Fermi surface of iron oxypnictides: Covalency and sensitivity to structural changes*, V. Vildosola, L. Pourovskii, R. Arita, S. Biermann, and A. Georges, Phys. Rev. B 78, 064518 (2008).

[16] *Density-functional calculation of the Coulomb repulsion and correlation strength in superconducting* LaFeAsO, V. I. Anisimov, D. M. Korotin, S. V. Streltsov, A. V. Kozhevnikov, J. Kunes, A. O. Shorikov, and M. A. Korotin, JETP Lett. 88, 729 (2008).

[17] *Ab initio Derivation of Low-Energy Model for Iron-Based Superconductors* LaFeAsO *and* LaFePO, K. Nakamura, R. Arita, and M. Imada, J. Phys. Soc. Jpn. 77, 093711 (2008).

[18] *Strength of correlations in pnictides and its assessment by theoretical calculations and spectroscopy experiments*, V. I. Anisimov, E. Z. Kurmaev, A. Moewes, I. A. Izyumov, Physica C 469, (2009)

[19] *Evidence for weak electronic correlations in iron pnictides*, W. L. Yang, A. P. Sorini, C. C. Chen, B. Moritz, W. S. Lee, F. Vernay, P. Olalde-Velasco, J. D. Denlinger, B. Delley, J. H. Chu, J. G. Analytis, I. R. Fisher, Z. A. Ren, J. Yang, W. Lu, Z. X. Zhao, J. van den Brink, Z. Hussain, Z. X. Shen and T. P. Devereaux, Phys. Rev. B 80, 014508 (2009).

[20] *Near-degeneracy of several pairing channels in multiorbital models for the Fe pnictides*, S. Graser, T. A. Maier, P. J. Hirschfeld and D. J. Scalapino, New J. Phys. 11, 025016 (2009).

[21] *Sensitivity of the superconducting state and magnetic susceptibility to key aspects of electronic structure in ferropnictides*, A. F. Kemper, T. A. Maier, S. Graser, H. P. Cheng, P. J. Hirschfeld and D. J. Scalapino, New J. Phys. 12, 073030 (2010).

[22] *Superconductivity at 55 K in iron-based F-doped layered quaternary compound* $Sm[O_{1-x}F_x]FeAs$ Z. A. Ren, W. Lu, J. Yang, W. Yi, X. L. Shen, Z. C. Li, G. C. Che, X. L. Dong, L. L. Sun, F. Zhou and Z. X. Zhao, Chin. Phys. Lett. 25, 2215 (2008).

[23] *Superconductivity and phase diagram in iron-based arsenic-oxides* $ReFeAsO_{1-\delta}$ *(Re = rare-earth metal) without fluorine doping* Z. A. Ren, G.-C. Che , X.-L. Dong , J. Yang , W. Lu , W. Yi , X.-L. Shen , Z.-C. Li , L.-L. Sun , F. Zhou and Z.-X. Zhao, Europhys. Lett. 83, 17002 (2008).

[24] *Thorium-doping-induced superconductivity up to 56 K in* $Gd_{1-x}Th_xFeAsO$ C. Wang, L. J. Li, S. Chi, Z. W. Zhu, Z. Ren, Y. K. Li, Y. T. Wang, X. Lin, Y. K. Luo, S. Jiang, X. F. Xu, G. H. Cao and Z. A. Xu, Europhys. Lett. 83, 67006 (2008).

[25] *High-*T_c *superconductivity induced by doping rare-earth elements into CaFeAsF*, Peng Cheng, Bing Shen, Gang Mu, Xiyu Zhu, Fei Han, Bin Zeng and Hai-Hu Wen, Europhys. Lett. 85, 67003 (2009).

[26] *Anisotropic thermodynamic and transport properties of single crystalline* $(Ba_{1-x}K_x)Fe_2As_2$ $(x = 0$ *and 0.45)*, N. Ni, S. L. Bud'ko, A. Kreyssig, S. Nandi, G. E. Rustan, A. I. Goldman, S. Gupta, J. D. Corbett, A. Kracher, P. C. Canfield, Phys. Rev. B 78, 014507 (2008).

[27] *Multiple phase transitions in single-crystalline* $Na_{1-\delta}FeAs$, G. F. Chen, W. Z. Hu, J. L. Luo, and N. L. Wang, Phys. Rev. Lett. 102, 227004 (2009).

[28] *Structural and magnetic phase transitions in* $Na_{1_\delta}FeAs$, S. Li, C. de la Cruz, Q. Huang, G. F. Chen, T. L. Xia, J. L. Luo, N. L. Wang, and P. Dai, Phys. Rev. B 80, 020504(R) (2009).

[29] *Electronic structure reconstruction: the driving force behind the magnetic and structural transitions in* NaFeAs, C. He, Y. Zhang, B. P. Xie, X. F. Wang, L. X. Yang, B. Zhou, F. Chen, M. Arita, K. Shimada, H. Namatame, M. Taniguchi, X. H. Chen, J. P. Hu, D. L. Feng, arXiv:1001.2981v1 [cond-mat.supr-con] (2010).

[30] *Crystal, spin, and electronic structure of the superconductor* LiFeAs, Z. Li, J. S. Tse, and C. Q. Jin, Phys. Rev. B 80, 092503 (2009).

[31] *Electronic structure and doping in* $BaFe_2As_2$ *and* LiFeAs*: Density functional calculations*, D. J. Singh, Phys. Rev. B78, 094511 (2008).

[32] *Striped antiferromagnetic order and electronic properties of stoichiometric* LiFeAs *from first-principles calculations*, Y. F. Li and B. G. Liu, Eur. Phys. J. B 72, 00338 (2009).

[33] *First-principles study of the magnetic, structural and electronic properties of* LiFeAs X. X. Zhang, H. Wang, and Y. M. Ma, J. Phys.: Condens. Matter 22, 046006 (2010).

[34] LiFeAs*: An intrinsic FeAs-based superconductor with* $T_c = 18\,K$, J. H. Tapp, Z. J. Tang, B. Lv, K. Sasmal, B. Lorenz, P. C. W. Chu, and A. M. Guloy, Phys. Rev. B 78, 060505 (2008).

[35] *Structure and superconductivity of* LiFeAs, M. J. Pitcher, D. R. Parker, P. Adamson, S. J. C. Herkelrath, A. T. Boothroyd, R. M. Ibberson, M. Brunelli and S. J. Clarke, Chem. Commun. 45, 5918 (2008).

[36] *The superconductivity at 18 K in* LiFeAs *system*, X. C. Wang, Q. Q. Liu, Y. X. Lv, W. B. Gao, L. X. Yang, R. C. Yu, F. Y. Li and C. Q. Jin, Solid State Commun. 148, 538 (2008).

[37] *Observation of Fermi surface-dependent nodeless superconducting gaps in* $Ba_{0.6}K_{0.4}Fe_2As_2$, H. Ding, P. Richard, K. Nakayama, K. Sugawara, T. Arakane, Y. Sekiba, A. Takayama, S. Souma, T. Sato, T. Takahashi, Z. Wang, X. Dai, Z. Fang, G. F. Chen, J. L. Luo and N. L. Wang, Europhys. Lett. 83, 47001 (2008).

[38] *Electron-Hole Asymmetry in Superconductivity of Pnictides Originated from the Observed Rigid Chemical Potential Shift*, M. Neupane, P. Richard, Y.-M. Xu, K. Nakayama, T. Sato, T. Takahashi, A. V. Fedorov, G. Xu, X. Dai, Z. Fang, Z. Wang, G.-F. Chen, N.-L. Wang, H.-H. Wen, H. Ding, arXiv:1005.2966v1 [cond-mat.supr-con] (2010).

[39] *Evidence for three-dimensional Fermi-surface topology of the layered electron-doped iron superconductor* $Ba(Fe_{1-x}Co_x)_2As_2$, P. Vilmercati, A. Fedorov, I. Vobornik, U. Manju, G. Panaccione, A. Goldoni, A. S. Sefat, M. A. McGuire, B. C. Sales, R. Jin, D. Mandrus, D. J. Singh, and N. Mannella, Phys. Rev. B 79, 220503(R) (2009).

[40] *Three-Dimensional Electronic Structure of Superconducting Iron Pnictides Observed by Angle-Resolved Photoemission Spectroscopy*, W. Malaeb, T. Yoshida, A. Fujimori, M. Kubota, K. Ono, K. Kihou, P. M. Shirage, H. Kito, A. Iyo, H. Eisaki, Y. Nakajima, T. Tamegai, and R Arita, J. Phys. Soc. Jpn. 78, 123706 (2009).

[41] *Orbital character variation of the Fermi surface and doping dependent changes of the dimensionality in* $BaFe_{2-x}Co_xAs_2$ *from angle-resolved photoemission spectroscopy*, S. Thirupathaiah, S. de Jong, R. Ovsyannikov, H. A. Duerr, A. Varykhalov, R. Follath, Y. Huang, R. Huisman, M. S. Golden, Y.-Z. Zhang, H. O. Jeschke, R. Valenti, A. Erb, A. Gloskovskii, J. Fink, Phys. Rev. B 81, 104512 (2010).

[42] *Observation of a ubiquitous three-dimensional superconducting gap function in optimally-doped* $Ba_{1-x}K_xFe_2As_2$, Y.-M. Xu, Y.-B. Huang, X.-Y. Cui, R. Elia, R. Milan, M. Shi, G.-F. Chen, P. Zheng, N.-L. Wang, P.-C. Dai, J.-P. Hu, Z. Wang, H. Ding, arXiv:1006.3958v1 [cond-mat.supr-con] (2010).

[43] *Unconventional Superconductivity with a Sign Reversal in the Order Parameter of* $LaFeAsO_{1-x}F_x$, I. I. Mazin, D. J. Singh, M. D. Johannes, and M. H. Du, Phys. Rev. Lett. 101, 057003 (2008).

[44] *Evidence for a Nodal-Line Superconducting State in* LaFePO, J. D. Fletcher, A. Serafin, L. Malone, J. G. Analytis, J.-H. Chu, A. S. Erickson, I. R. Fisher, and A. Carrington, Phys. Rev. Lett. 102, 147001 (2009).

[45] *Neutron scattering resonance and the iron-pnictide superconducting gap*, T. A. Maier, S. Graser, D. J. Scalapino, and P. Hirschfeld, Phys. Rev. B 79, 134520 (2009).

[46] *Sensitivity of the superconducting state and magnetic susceptibility to key aspects of electronic structure in ferropnictides*, A. F. Kemper, T. A. Maier, S. Graser, H.-P. Cheng, P. J. Hirschfeld, D. J. Scalapino, arXiv:1003.2777v3 [cond-mat.supr-con] (2010).

[47] *Experimental determination of the microscopic origin of magnetism in parent iron pnictides*, D. Hsieh, Y. Xia, L. Wray, D. Qian, K. Gomes, A. Yazdani, G. F. Chen, J. L. Luo, N. L. Wang, M. Z. Hasan, arXiv:0812.2289v1 [cond-mat.supr-con] (2008).

[48] *Orbital-Dependent Modifications of Electronic Structure across the Magnetostructural Transition in* $BaFe_2As_2$, T. Shimojima, K. Ishizaka, Y. Ishida, N. Katayama, K. Ohgushi, T. Kiss, M. Okawa, T. Togashi, X. -Y. Wang, C. -T. Chen, S. Watanabe, R. Kadota, T. Oguchi, A. Chainani, S. Shin, Phys. Rev. Lett. 104, 057002 (2010).

[49] *Electronic structure of the* $BaFe_2As_2$ *family of iron-pnictide superconductors*, M. Yi, D. H. Lu, J. G. Analytis, J.-H. Chu, S.-K. Mo, R.-H. He, R. G. Moore, X. J. Zhou, G. F. Chen, J. L. Luo, N. L. Wang, Z. Hussain, D. J. Singh, I. R. Fisher, and Z.-X. Shen, Phys. Rev. B 80, 024515 (2009).

[50] *The orbital characters of bands in iron-based superconductor* $BaFe_{1.85}Co_{0.15}As_2$, Y. Zhang, B. Zhou, F. Chen, J. Wei, M. Xu, L. X. Yang, C. Fang, W. F. Tsai, G. H. Cao, Z. A. Xu, M. Arita, C.H. Hong, K. Shimada, H. Namatame, M. Taniguchi, J. P. Hu, D. L. Feng, arXiv:0904.4022v1 [cond-mat.supr-con] (2009).

[51] *Crystal symmetry and magnetic order in iron pnictides: A tight-binding Wannier function analysis*, Z. P. Yin and W. E. Pickett, Phys. Rev. B 81, 174534 (2010).

[52] *Multiorbital Effects on Antiferromagnetism in Fe Pnictides*, K. Kubo and P. Thalmeier, J. Phys. Soc. Jpn. 78, 083704 (2009).

[53] *Doping Dependence of an n-Type Cuprate Superconductor Investigated by Angle-Resolved Photoemission Spectroscopy*, N. P. Armitage, F. Ronning, D. H. Lu, C. Kim, A. Damascelli, K. M. Shen, D. L. Feng, H. Eisaki, and Z.-X. Shen, Phys. Rev. Lett. 88, 257001 (2002).

[54] *Unconventional electronic reconstruc- tion in undoped* $(Ba, Sr)Fe_2As_2$ *across the spin density wave transition*, M. Yi, D.H. Lu, J.G. Analytis, J.-H. Chu, S.-K. Mo, R.-H. He, M. Hashimoto, R.G. Moore, I.I. Mazin, D.J. Singh, Z. Hussain, I.R. Fisher, and Z.-X. Shen, Phys. Rev. B 80, 174510 (2009).

[55] *Coexistence of static magnetism and superconductivity in* $SmFeAsO_{1-x}F_x$ *as revealed by muon spin rotation*, A. J. Drew, C. Niedermayer, P. J. Baker, F. L. Pratt, S. J. Blundell, T. Lancaster, R. H. Liu, G. Wu, X. H. Chen, I. Watanabe, V. K. Malik, A. Dubroka, M. Rössle, K. W. Kim, C. Baines and C. Bernhard, Nature Materials 8-2396, 310-314, (2009).

[56] *Theory of magnetic fluctuations in iron pnictides*, L. Craco and M. S. Laad, Phys. Rev. B 80, 054520 (2009).

[57] *Spin excitations in* $BaFe_{1.84}Co_{0.16}As_2$ *superconductor observed by inelastic neutron scattering*, D. Parshall, K. A. Lokshin, J. Niedziela, A. D. Christianson, M. D. Lumsden, H. A. Mook, S. E. Nagler, M. A. McGuire, M. B. Stone, D. L. Abernathy, A. S. Sefat, B. C. Sales, D. G. Mandrus, and T. Egami, Phys. Rev. B 80, 012502 (2009).

[58] *Unconventional superconductivity in* $Ba_{0.6}K_{0.4}Fe_2As_2$ *from inelastic neutron scattering*, A. D. Christianson, E. A. Goremychkin, R. Osborn, S. Rosenkranz, M. D. Lumsden, C. D. Malliakas, I. S. Todorov, H. Claus, D. Y. Chung, M. G. Kanatzidis, R. I. Bewley and T. Guidi, Nature 456, 07625 (2008).

[59] *BCS primer: A guide to computational methods in superconductivity theory*, D. Sahu, A. Langner and T. F. George, J. Chem. Educ., 67 (9), p 738 (1990).

[60] *Angle-Resolved Photoelectron Spectroscopy Studies of the Many-Body Effects in the Electronic Structure of High-Tc Cuprates*, D. S. Isonov, PhD Thesis, IFW Dresden, 2008.

[61] S. Hüfner, Photoelectron Spectroscopy, Principles and Applications, Springer-Verlag, Berlin Heidelberg, 2nd Edition, 1996.

[62] *Superconductivity at 23 K in Pt doped* $BaFe_2As_2$ *single crystals*, S. R. Saha, T. Drye, K. Kirshenbaum, N. P. Butch, P. Y. Zavalij, J.-P. Paglione, J. Phys.: Condens. Matter 22, 072204 (2010).

[63] *Orbital Character Simulation using Selection Rules*, X.-P. Wang, unpublished (ongoing project).

[64] *Iron-Pnictide and Cuprate High-temperature Superconductors Investigated by Photoemission Spectroscopy*, W. Malaeb, PhD Thesis, Department of complexity science and engineering, University of Tokyo, 2009.